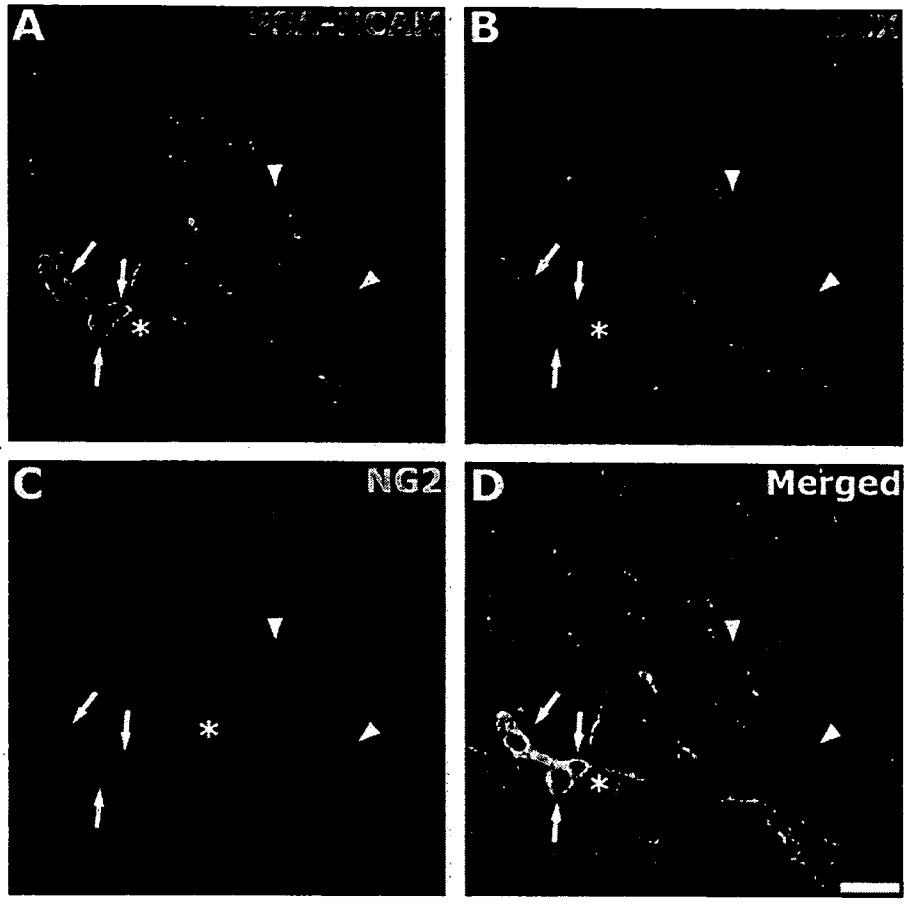

FIG. 3. Doublecortin (DCX)(+)/NG2(+) cells were a different population from DCX(+)/polysialyated form of neural cell adhesion molecule (PSA-NCAM)(+) cells in the piriform cortex. (A–D) Triple immunohistochemistry for PSA-NCAM (green), DCX (red) and NG2 (blue) in the piriform cortex. Arrowheads, DCX(+)/NG2(+) cells not immunopositive for PSA-NCAM; arrows, DCX(+)/PSA-NCAM(+) cells not immunopositive for NG2. Asterisks, DCX(+) cell not immunopositive for NG2 nor PSA-NCAM (referred to in Nacher *et al.*, 2001). Scale bar: 20 μm.

TABLE 1. Percentages of cells immunopositive for various cell differentiation markers in all BrdU-labeled cells

	BrdU-labeled cells immunopositive for each marker after injection of BrdU (%)		
	After 2 h	After 14 days	After 28 days
DCX(+)/NG2(+)	94.2 ± 1.8 (450/479)	79.5 ± 3.8 (932/1168)	69.4 ± 3.2 (584/843)
DCX(+)/NG2(–)	0 (0/479)	0.61 ± 0.44 (7/1168)	0.52 ± 0.69 (4/843)
DCX(–)/NG2(+)	0 (0/479)	9.5 ± 3.4 (112/1168)	11.0 ± 1.8 (95/843)
NG2(+)/GST-pi(+)	0 (0/213)	10.2 ± 2.6 (52/519)	12.4 ± 2.8 (48/373)
NG2(–)/GST-pi(+)	0 (0/213)	0 (0/519)	9.2 ± 1.2 (35/373)

Data are presented as mean ± SEM (%), $n = 5$ animals at each time point. The number of positive cells for each marker/number of BrdU-labeled cells is given in parentheses. DCX, doublecortin; GST, glutathione S-transferase.

1989), another mature oligodendrocyte marker, revealed that this immunoreactivity was detected in most of the DCX(–)/NG2(–)/GST-pi(+) cells (Fig. 6I–K).

Discussion

In the present study, we have provided novel evidence that the adult rat neocortex ubiquitously possesses DCX(+)/NG2(+) cells and that these cells are the major population of cortical cells involved in cell reproduction. The DCX(+)/NG2(+) cells differentiate into two kinds of cell lineages [DCX(+)/NG2(–) cells and DCX(–)/NG2(+) cells] at 14–28 days after mitosis, as well as undergoing reproduction into identical cells. DCX(+)/NG2(–) cells were immunoreactive for TUC-4, a neuronal lineage marker, whereas DCX(–)/NG2(+) cells started to co-express an oligodendrocyte marker GST-pi. Furthermore, the NG2(+)/GST-pi(+) cells differentiated into new mature oligodendrocytes at 28 days. These results indicate that the DCX(+)/NG2(+) cells serve as cortical progenitor cells, retaining the potential to produce neuronal lineage cells and oligodendrocytes in the neocortex (Fig. 7).

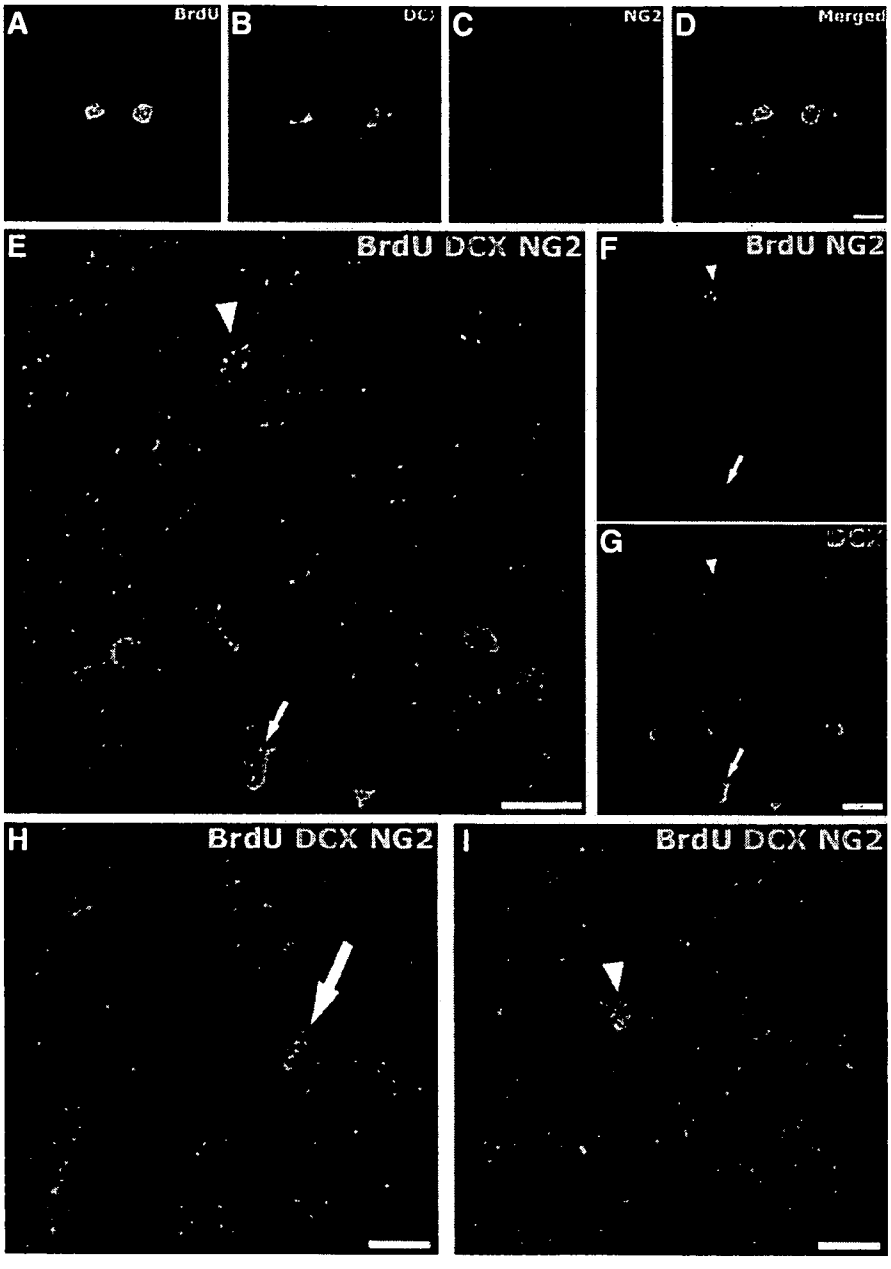

FIG. 4. (A–D) 5′-Bromodeoxyuridine (BrdU)-incorporated nuclei (green) in NG2(+)/doublecortin (DCX)(+) cells in the neocortex at 2 h after BrdU injection: (red), DCX; (blue), NG2. (E–I) Multi-differentiation of BrdU-labeled NG2(+)/DCX(+) cells in the neocortex at 14 days after BrdU injection: BrdU (green), DCX (red) and NG2 (blue). Arrowheads in (E–G), BrdU-labeled DCX(+)/NG2(–) cells; (E–G) indicate the same area. Small arrows in (E–G), a BrdU-labeled DCX(+)/NG2(+) cell. Big arrow in (H), a BrdU-labeled DCX(–)/NG2(+) cell. Scale bars: 10 μm (A–D); 20 μm (E–I).

Two subtypes of NG2-positive cells in the neocortex of adult rats

It has been known that NG2(+) cells abundantly and broadly exist in the cerebral cortex of adult rats. We observed that 1.2 ± 0.4% and 1.8 ± 0.7% of NG2(+) cells (813 cells and 946 cells from five animals) in the neocortex were immunoreactive for BrdU and Ki67, respectively, 2 h after BrdU injection. The findings suggested that few cortical NG2(+) cells are involved in the cell cycle, and are supported by a previous report that only 1.5% of all NG2-positive cells are labeled with BrdU 2 h after BrdU injection (Dawson *et al.*, 2003). In the spinal cord of adult rats, two subtypes of NG2-positive cells were argued based on their response to experimental demyelination (Keirstead *et al.*, 1998). Thus, we assumed that two distinct populations of NG2(+) cells were also present in the adult cortex, and confirmed this finding based on co-expression of DCX (Fig. 2). Proliferative activity was observed only in the DCX(+)/NG2(+) cells, but not in the DCX(–)/NG2(+) cells (Fig. 4D). Furthermore, we confirmed that none of the DCX(+)/NG2(+) cells in the neocortex was immunopositive for GFAP or nestin. Our previous studies showed that the majority of proliferating cells are located close to the neuronal somata (the perineuronal territory) in the cerebral cortex of adult rats (Kataoka *et al.*, 2006). Indeed, in the present study, most of the

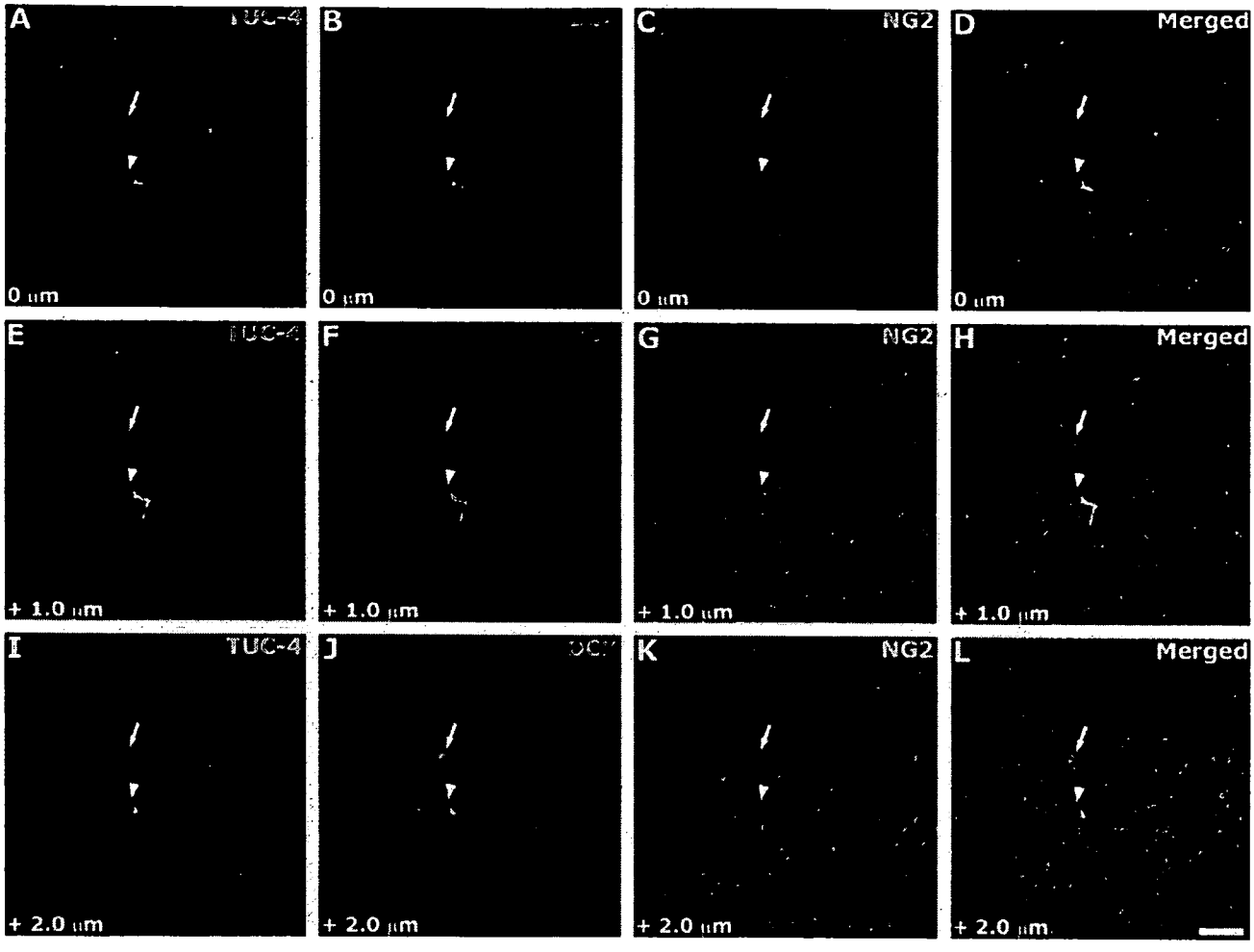

FIG. 5. A neuronal lineage marker (TUC-4)-expressing doublecortin (DCX)(+)/NG2(–) cells. Sequential confocal images (0 to +2 μm; A–D, 0μm; E–H, +1.0μm; I–L, +2.0μm) captured at 1-μm intervals for TUC-4 (green), DCX (red) and NG2 (blue). Arrowheads, DCX(+)/NG2(–) cells immunopositive for TUC-4; arrows, DCX(+)/NG2(+) cells not immunopositive for TUC-4. Scale bar: 20 μm.

DCX(+)/NG2(+) cells were observed in the perineuronal territory, and many DCX(–)/NG2(+) cells were outside this area (data not shown). These findings suggest that the DCX(+)/NG2(+) cells are 'cortical progenitor cells' in the neocortex.

Existence of DCX(+) cells in the adult neocortex

In the present study, we observed that the DCX(+)/NG2(+) cells exist throughout the neocortex of adult rats under physiological conditions (Fig. 2). However, previous studies in adult rats have reported that DCX(+) cells are observed only in cortical layers II or III of the piriform cortex, and in layer II of the entorhinal, perirhinal and insular cortex (Nacher *et al.*, 2001, 2004), but not in the neocortex more dorsal to these regions (Jin *et al.*, 2003; Yang *et al.*, 2004; Dayer *et al.*, 2005). Indeed, the intensity of DCX immunoreactivity in the DCX(+)/NG2(+) cells observed in the present study was weaker than that in the previously reported DCX(+) cells in the piriform cortex (Fig. 3D). Thus, we could barely immunodetect DCX in the DCX(+)/NG2(+) cells at lower magnifications using a confocal laser-scanning microscope; however, we were able to successfully detect them at higher magnifications, i.e. ×40 or ×63 at the objective lens. Furthermore, we confirmed the expression of DCX in the neocortex using Western blot analysis; a single 40-kDa band of DCX protein (Brown *et al.*, 2003) was detected in tissue homogenates prepared from the parietal cortical tissue as well as piriform cortex (data not shown).

Cellular differentiation of the DCX(+)/NG2(+) cells

In the current study, we showed that DCX(+)/NG2(–) cells are generated from DCX(+)/NG2(+) cells in the neocortex of adult rats using BrdU-labeling methods (Fig. 4 and Table 1), and that all the DCX(+)/NG2(–) cells contain TUC-4 (Fig. 5). In the dentate gyrus of the hippocampus, it has been shown that a subset of NG2(+) cells can differentiate into GABAergic neurons, upregulating the expression of TOAD-64 (referred to as TUC-4) and downregulating the expression of NG2 (Belachew *et al.*, 2003). We confirmed that the NG2(+) cells in the dentate gyrus were also immunoreactive for DCX (data not shown). Furthermore, DCX-expressing NG2(+) progenitor cells are also observed in the anterior SVZ, and these cells differentiate into GABAergic interneurons in the olfactory bulb. Such NG2(+) cells of these neurogenic regions differentiate into GABAergic interneurons following downregulation of the NG2 expression (Aguirre & Gallo, 2004). The possibility exists that the DCX(+)/NG2(+) cells in the

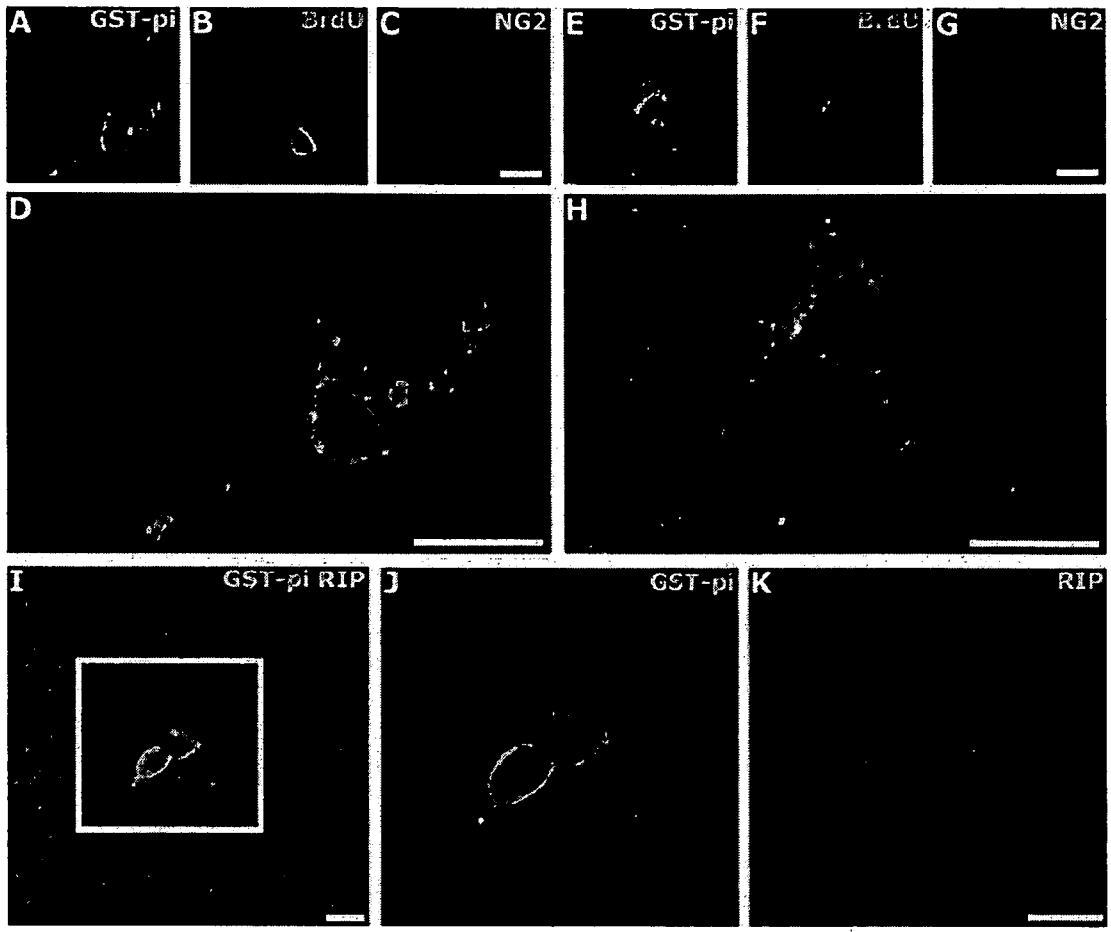

FIG. 6. Glial lineage markers expressing DCX(–)/NG2(+) cells. (A–D) A 5′-bromodeoxyuridine (BrdU)-labeled NG2(+)/glutathione S-transferase (GST)-pi(+) cell in the neocortex at 14 days after BrdU injection. (E–H) A BrdU-labeled NG2(–)/GST-pi(+) cell in the neocortex at 28 days after BrdU injection: GST-pi (green), BrdU (red) and NG2 (blue). (I–K) Two GST-pi(+)/RIP(+) cells in the neocortex, GST-pi (green) and RIP (blue). (G and K) Magnified views of the area indicated by a white square in (I). Scale bars: 10 μm.

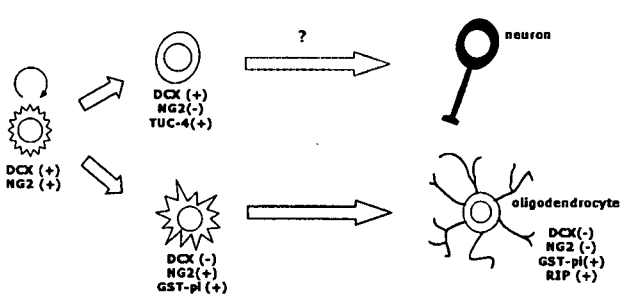

FIG. 7. Schematic representation of a hypothetical differentiation model of doublecortin (DCX)(+)/NG2(+) cells in the adult neocortex. DCX(+)/NG2(+) cells reproduce the identical cells, DCX(+)/NG2(–) cells and DCX(+)/NG2(–) cells. In the neuronal lineage, newly generated DCX(+)/NG2(–) cells show TUC-4 immunoreactivity. In the oligodendrocyte differentiation, newly generated DCX(–)/NG2(+) cells show glutathione S-transferase (GST)-pi immunoreactivity, and the cells further differentiate into mature oligodendrocytes immunopositive for GST-pi and RIP. During oligodendrocyte differentiation, the expression of NG2 is downregulated, whereas that of cytoplasmic GST-pi is upregulated.

adult neocortex also differentiate into GABAergic interneurons with downregulation of NG2 expression. In the present study, we were able to demonstrate that neocortical DCX(+)/NG2(+) cells have the potential to give rise to DCX(+)/NG2(–) cells committed to neuronal lineage cells, but found that none of the cells indicated immunohistochemical characteristics of mature GABAergic neurons. Under such a low-stimulative environment as in the present experiment, rodent neocortex might not need to generate new neurons. In fact, it has been reported that neurogenesis occurs in the cerebral cortex of adult mice under pathological conditions (Magavi *et al.*, 2000). Furthermore, in the present study we were unable to determine the fates and functions of newly generated DCX(+)/NG2(–) cells in the neocortex. Although those cells were not immunohistochemically mature neurons, such neuronal lineage cells might have physiological functions even at immature stages. A subpopulation of immature cells in the cortex has been reported to show physiological properties, including ion channel expression profiles and depolarization-induced multiple spikes (Chittajallu *et al.*, 2004).

At 2 h after BrdU injection, a small number of dividing cells were OX-42(+) microglia. Thus, we cannot rule out the possibility that the DCX(+)/NG2(–) cells were generated from the microglia *in situ* in the neocortex. However, until now microglia has not been reported to give rise to neurons or other glial cells, including astrocytes, oligodendrocytes and NG2(+) glial progenitor cells in the adult brain under physiological conditions. Indeed, we observed that none of the OX-42(+) cells was immunoreactive for NG2 and/or DCX in the

neocortex. The origin of the newly generated DCX(+)/NG2(–) cells may be related to BrdU(+)/DCX(+) cells originating in the SVZ migrating into the neocortex under pathological conditions, as shown by Magavi *et al.* (2000). In the neonatal brain, newly generated DCX(+) cells have also been reported to migrate from the SVZ to the cerebral cortex (Suzuki & Goldman, 2003; Fagel *et al.*, 2006). The vast majority of the DCX(+) young neurons migrating from the SVZ have been known to express PSA-NCAM (Doetsch *et al.*, 1997, 1999; Fagel *et al.*, 2006). However, the newly generated DCX(+)/NG2(–) cells observed in the present study were not immunopositive for PSA-NCAM (data not shown). Based on these findings we suggest that the DCX(+)/NG2(–) cells were likely derived from the DCX(+)/NG2(+) cells *in situ* in the neocortical parenchyma.

Dawson *et al.* (2003) suggested that cortical NG2(+) cells can generate new oligodendrocytes, by finding BrdU-labeled cells expressing 2′,3′-cyclic nucleotide 3′-phosphodiesterase (CNPase), an oligodendrocyte marker. However, that study did not trace the differentiation between NG2-expressing cells and CNPase-expressing mature oligodendrocytes, and could not show that NG2(+) cells were on the identical cell lineage path of mature oligodendrocytes. In the present study, using GST-pi, an oligodendrocyte lineage marker, we were able to trace every stage of oligodendrocyte differentiation by NG2(+)/GST-pi(+) cells from DCX(+)/NG2(+) progenitor cells to NG2(–)/GST-pi(+) mature oligodendrocytes (Fig. 6A–H and Table 1). The NG2(–)/GST-pi(+) cells were confirmed to be mature oligodendrocytes by observation of immunoreactivity for RIP, a mature oligodendrocyte marker (Fig. 6I). These results are in agreement with previous reports indicating maturation of oligodendrocytes following the downregulation of NG2 expression (Nishiyama *et al.*, 1996) and the progressive expression of RIP (Friedman *et al.*, 1989). We have provided the first evidence that cortical NG2(+) cells co-expressing a neuronal marker reproduce mature oligodendrocytes.

It has been reported that NG2(+) cells may give rise to GFAP(+) astrocytes in the cerebral cortex of adult rats (Dawson *et al.*, 2003). In the present study, BrdU-labeled GFAP(+) astrocytes were infrequently found in the adult neocortex at 28 days after BrdU injection (less than 1%, 2/456 cells from five animals). Thus, perineuronal DCX(+)/NG2(+) cells might differentiate into astrocytes as well as oligodendrocytes and neurons. We previously demonstrated that neural excitation stimulates cellular proliferation of the perineuronal cells (Tamura *et al.*, 2004; Kataoka *et al.*, 2006), and such an excitation facilitates the production of GFAP(+) astrocytes (unpublished observation). These observations suggest that local neural activity controls the production rates of astrocytes, oligodendrocytes and neurons by regulating the proliferation rate and the direction of the differentiation of the DCX(+)/NG2(+) cells.

Acknowledgements

This work was supported in part by Special Coordination Funds for Promoting Science and Technology from the Ministry of Education, Culture, Sports, Science and Technology, Japan to Y.K., by a consignment expense from the Molecular Imaging Program on 'Research Base for Exploring New Drugs' from the Ministry of Education, Culture, Sports, Science and Technology to Y.W., and by a Grant-in-Aid for Scientific Research from the Japan Society for Promotion of Science to Y.K. and H.Y.

Abbreviations

BrdU, 5′-bromodeoxyuridine; CNPase, 2′,3′-cyclic nucleotide 3′-phosphodiesterase; DCX, doublecortin; GABA, γ-aminobutyric acid; GFAP, glial fibrillary acidic protein; GST, glutathione S-transferase; PBS, phosphate-buffered saline; PBST, 0.3% Triton X-100 in PBS; PSA-NCAM, polysialyated form of neural cell adhesion molecule; SVZ, subventricular zone.

References

Aguirre, A. & Gallo, V. (2004) Postnatal neurogenesis and gliogenesis in the olfactory bulb from NG2-expressing progenitors of the subventricular zone. *J. Neurosci.*, **24**, 10530–10541.

Belachew, S., Chittajallu, R., Aguirre, A.A., Yuan, X., Kirby, M., Anderson, S. & Gallo, V. (2003) Postnatal NG2 proteoglycan-expressing progenitor cells are intrinsically multipotent and generate functional neurons. *J. Cell Biol.*, **161**, 169–186.

Brown, J.P., Couillard-Despres, S., Cooper-Kuhn, C.M., Winkler, J., Aigner, L. & Kuhn, H.G. (2003) Transient expression of doublecortin during adult neurogenesis. *J. Comp. Neurol.*, **467**, 1–10.

Cameron, H.A., Woolley, C.S., McEwen, B.S. & Gould, E. (1993) Differentiation of newly born neurons and glia in the dentate gyrus of the adult rat. *Neuroscience*, **56**, 337–344.

Chittajallu, R., Aguirre, A. & Gallo, V. (2004) NG2-positive cells in the mouse white and grey matter display distinct physiological properties. *J. Physiol.*, **561**, 109–122.

Dawson, M.R., Polito, A., Levine, J.M. & Reynolds, R. (2003) NG2-expressing glial progenitor cells: an abundant and widespread population of cycling cells in the adult rat CNS. *Mol. Cell. Neurosci.*, **24**, 476–488.

Dayer, A.G., Cleaver, K.M., Abouantoun, T. & Cameron, H.A. (2005) New GABAergic interneurons in the adult neocortex and striatum are generated from different precursors. *J. Cell Biol.*, **168**, 415–427.

Doetsch, F., Caille, I., Lim, D.A., Garcia-Verdugo, J.M. & Alvarez-Buylla, A. (1999) Subventricular zone astrocytes are neural stem cells in the adult mammalian brain. *Cell*, **97**, 703–716.

Doetsch, F., Garcia-Verdugo, J.M. & Alvarez-Buylla, A. (1997) Cellular composition and three-dimensional organization of the subventricular germinal zone in the adult mammalian brain. *J. Neurosci.*, **17**, 5046–5061.

Doetsch, F., Petreanu, L., Caille, I., Garcia-Verdugo, J.M. & Alvarez-Buylla, A. (2002) EGF converts transit-amplifying neurogenic precursors in the adult brain into multipotent stem cells. *Neuron*, **36**, 1021–1034.

Fagel, D.M., Ganat, Y., Silbereis, J., Ebbitt, T., Stewart, W., Zhang, H., Ment, L.R. & Vaccarino, F.M. (2006) Cortical neurogenesis enhanced by chronic perinatal hypoxia. *Exp. Neurol.*, **199**, 77–91.

Friedman, B., Hockfield, S., Black, J.A., Woodruff, K.A. & Waxman, S.G. (1989) In situ demonstration of mature oligodendrocytes and their processes: an immunocytochemical study with a new monoclonal antibody, rip. *Glia*, **2**, 380–390.

Gage, F.H., Coates, P.W., Palmer, T.D., Kuhn, H.G., Fisher, L.J., Suhonen, J.O., Peterson, D.A., Suhr, S.T. & Ray, J. (1995) Survival and differentiation of adult neuronal progenitor cells transplanted to the adult brain. *Proc. Natl Acad. Sci. USA*, **92**, 11879–11883.

Gritti, A., Frolichsthal-Schoeller, P., Galli, R., Parati, E.A., Cova, L., Pagano, S.F., Bjornson, C.R. & Vescovi, A.L. (1999) Epidermal and fibroblast growth factors behave as mitogenic regulators for a single multipotent stem cell-like population from the subventricular region of the adult mouse forebrain. *J. Neurosci.*, **19**, 3287–3297.

Jin, K., Sun, Y., Xie, L., Peel, A., Mao, X.O., Batteur, S. & Greenberg, D.A. (2003) Directed migration of neuronal precursors into the ischemic cerebral cortex and striatum. *Mol. Cell. Neurosci.*, **24**, 171–189.

Kataoka, Y., Tamura, Y., Takamori, Y., Cui, Y. & Yamada, H. (2006) Perineuronal germinal cells in the rat cerebral cortex. *Med. Mol. Morph.*, **39**, 28–32.

Keirstead, H.S., Levine, J.M. & Blakemore, W.F. (1998) Response of the oligodendrocyte progenitor cell population (defined by NG2 labelling) to demyelination of the adult spinal cord. *Glia*, **22**, 161–170.

Lois, C. & Alvarez-Buylla, A. (1993) Proliferating subventricular zone cells in the adult mammalian forebrain can differentiate into neurons and glia. *Proc. Natl Acad. Sci. USA*, **90**, 2074–2077.

Magavi, S.S., Leavitt, B.R. & Macklis, J.D. (2000) Induction of neurogenesis in the neocortex of adult mice. *Nature*, **405**, 951–955.

Morshead, C.M., Reynolds, B.A., Craig, C.G., McBurney, M.W., Staines, W.A., Morassutti, D., Weiss, S. & van der Kooy, D. (1994) Neural stem cells in the adult mammalian forebrain: a relatively quiescent subpopulation of subependymal cells. *Neuron*, **13**, 1071–1082.

Nacher, J., Crespo, C. & McEwen, B.S. (2001) Doublecortin expression in the adult rat telencephalon. *Eur. J. Neurosci.*, **14**, 629–644.

Nacher, J., Pham, K., Gil-Fernandez, V. & McEwen, B.S. (2004) Chronic restraint stress and chronic corticosterone treatment modulate differentially the expression of molecules related to structural plasticity in the adult rat piriform cortex. *Neuroscience*, **126**, 503–509.

Nishiyama, A., Chang, A. & Trapp, B.D. (1999) NG2+ glial cells: a novel glial cell population in the adult brain. *J. Neuropathol. Exp. Neurol.*, **58**, 1113–1124.

Nishiyama, A., Lin, X.H., Giese, N., Heldin, C.H. & Stallcup, W.B. (1996) Interaction between NG2 proteoglycan and PDGF alpha-receptor on O2A progenitor cells is required for optimal response to PDGF. *J. Neurosci. Res.*, **43**, 315–330.

Palmer, T.D., Markakis, E.A., Willhoite, A.R., Safar, F. & Gage, F.H. (1999) Fibroblast growth factor-2 activates a latent neurogenic program in neural stem cells from diverse regions of the adult CNS. *J. Neurosci.*, **19**, 8487–8497.

Paxinos, G. & Watson, C. (1998) *The Rat Brain in Stereotaxic Coordinates*, 4th Edn. Academic Press, San Diego.

Seki, T. (2002) Expression patterns of immature neuronal markers PSA-NCAM, CRMP-4 and NeuroD in the hippocampus of young adult and aged rodents. *J. Neurosci. Res.*, **70**, 327–334.

Seki, T. & Arai, Y. (1991) Expression of highly polysialylated NCAM in the neocortex and piriform cortex of the developing and the adult rat. *Anat. Embryol. (Berl.)*, **184**, 395–401.

Seri, B., Garcia-Verdugo, J.M., McEwen, B.S. & Alvarez-Buylla, A. (2001) Astrocytes give rise to new neurons in the adult mammalian hippocampus. *J. Neurosci.*, **21**, 7153–7160.

Suzuki, S.O. & Goldman, J.E. (2003) Multiple cell populations in the early postnatal subventricular zone take distinct migratory pathways: a dynamic study of glial and neuronal progenitor migration. *J. Neurosci.*, **23**, 4240–4250.

Tamura, Y., Kataoka, Y., Cui, Y. & Yamada, H. (2004) Cellular proliferation in the cerebral cortex following neural excitation in rats. *Neurosci. Res.*, **50**, 129–133.

Yang, H.K., Sundholm-Peters, N.L., Goings, G.E., Walker, A.S., Hyland, K. & Szele, F.G. (2004) Distribution of doublecortin expressing cells near the lateral ventricles in the adult mouse brain. *J. Neurosci. Res.*, **76**, 282–295.

Neuroscience 148 (2007) 535–540

INTRACELLULAR TRANSLOCATION OF GLUTATHIONE S-TRANSFERASE PI DURING OLIGODENDROCYTE DIFFERENTIATION IN ADULT RAT CEREBRAL CORTEX *IN VIVO*

Y. TAMURA,[a,b,c] Y. KATAOKA,[a,b,c]* Y. CUI,[a,b,c] Y. TAKAMORI,[a] Y. WATANABE[b,c] AND H. YAMADA[a]

[a]*Department of Anatomy and Cell Science, KMU 21C COE Project, Kansai Medical University, 10-15 Fumizono-cho, Moriguchi, Osaka 570-8506, Japan*

[b]*Molecular Imaging Research Program, Frontier Research System, RIKEN, 6-7-3 Minatojima minamimachi, Chuo-ku, Kobe 650-0047, Japan*

[c]*Department of Physiology, Osaka City University Graduate School of Medicine, 1-4-3 Asahimachi, Abeno-ku, Osaka 545-8585, Japan*

Abstract—Glutathione S-transferase (GST)-pi is a cytosolic isoenzyme used as a marker for mature oligodendrocytes in the mammalian brain. However, the cellular properties of GST-pi-immunoreactive [GST-pi (+)] cells in adult brain are not completely understood. We immunohistochemically demonstrated the existence of two subtypes of GST-pi (+) cells in the cerebral cortex of adult rats: one subtype exhibited GST-pi in the cytoplasm (C-type cells), while the other did mainly in the nucleus (N-type cells). The GST-pi (+) C-type cells were also immunopositive for 2′,3′-cyclic nucleotide 3′-phosphodiesterase and RIP, indicating that they were mature oligodendrocytes, while the GST-pi (+) N-type cells expressed NG2, indicating that they were oligodendrocyte progenitor cells. Furthermore, observation of the fate of newly-generated cells by 5-bromodeoxyuridine-labeling revealed that the GST-pi (+) N-type cells differentiated into C-type cells. These findings indicate translocation of GST-pi from the nucleus to the cytoplasm during oligodendrocyte maturation.

Key words: oligodendrocyte progenitor cells, NG2, CNPase, RIP, BrdU.

Glutathione S-transferases (GSTs) are phase II detoxification enzymes that catalyze the conjugation of various xenobiotic and endogenous electrophiles with reduced glutathione. The mammalian GSTs consist of eight distinct classes (alpha, mu, pi, theta, sigma, kappa, zeta, and omega) separable on the basis of their biological properties (Mannervik et al., 1985; Meyer et al., 1991; Meyer and Thomas, 1995; Pemble et al., 1996; Board et al., 1997, 2000). The GST isoenzymes are widely expressed and distributed among several types of tissue including the brain (Theodore et al., 1985; Li et al., 1986; Abramovitz and Listowsky, 1987). Three GST isoenzymes (alpha, mu, and pi) have been observed in neurons and glial cells in the brain: GST-alpha is expressed in the nuclei of neurons of the rat brain (Johnson et al., 1993); GST-mu is expressed in glial fibrillary acidic protein (GFAP)–immunopositive astrocytes, but in neither neurons nor oligodendrocytes in rat brain (Abramovitz et al., 1988; Cammer and Zhang, 1992); and GST-pi is found in the cytoplasm of mature oligodendrocytes, which are immunopositive for 2′,3′-cyclic nucleotide 3′-phosphodiesterase (CNPase), in rodent cerebral cortex (Cammer et al., 1989; Tansey and Cammer, 1991). Of these three GSTs, GST-pi has been used as a specific marker protein for mature oligodendrocytes in the mammalian adult brain (Tanaka et al., 2003; Mason et al., 2004; Gotts and Chesselet, 2005). However, it was recently reported that glial cells containing GST-pi protein in both the cytoplasm and nucleus were observed in the gray and white matter of normal human brain (Terrier et al., 1990). Thus, the properties of these GST-pi (+) cells have yet to be determined.

In the present study, we investigated the properties of GST-pi (+) C-type cells and GST (+) N-type cells using several specific markers of the oligodendrocyte lineage, including differentiation state-specific markers. Furthermore, cell differentiation processes in this lineage were observed using a flash labeling method with 5-bromodeoxyuridine (BrdU).

EXPERIMENTAL PROCEDURES

Animals and BrdU injections

Adult male Wistar rats (SLC, Hamamatsu, Japan; 250–350 g body weight) were used. All experimental protocols were approved by the Ethics Committee on Animal Care and Use of Kansai Medical University and were performed in accordance with the Principles of Laboratory Animal Care (NIH Publication No. 85–23, revised 1985). Every effort was made to minimize the number of animals used and their suffering. In order to label proliferating cells, rats (n=9) were intraperitoneally injected with BrdU diluted with saline (50 mg/kg body weight).

Histochemistry

Animals were deeply anesthetized with diethyl ether and perfused transcardially with 4% formaldehyde buffered with 0.1 M phosphate-buffered saline (PBS; pH 7.4) 2 h, 14 days, and 28 days after BrdU injection. The brains were removed, post-fixed in 4% formaldehyde buffered with 0.1 M PBS overnight at 4 °C, and then immersed in 20% (w/v) sucrose solution. Coronal brain sections

*Correspondence to: Y. Kataoka, Department of Physiology, Osaka City University Graduate School of Medicine, 1-4-3 Asahimachi, Abeno-ku, Osaka 545–8585, Japan. Tel: +81-6-6645-3711; fax: +81-6-6645-3712.
E-mail address: kataokay@med.osaka-cu.ac.jp (Y. Kataoka).

Abbreviations: BrdU, 5-bromodeoxyuridine; CNPase, 2′,3′-cyclic nucleotide 3′-phosphodiesterase; GST, glutathione S-transferase; PBS, phosphate-buffered saline; PBST, 0.3% Triton X-100 in phosphate-buffered saline.

0306-4522/07$30.00+0.00
doi:10.1016/j.neuroscience.2007.06.026

Fig. 1. Two subtypes of GST-pi (+) cells in cerebral cortex. (A) Double staining for GST-pi (green) and TO-PRO3 (red) in cortical layers I and II–III of somatosensory cortex reveals two subtypes of GST-pi (+) cells; arrows indicate cytoplasmic GST-pi (+) cells, while the arrowhead indicates a nuclear GST-pi (+) cell on the image of a single z-slice. (B, C) Single-z-slice images with ortho-images of confocal z-stacks (upper and right panels in B and C) of GST-pi (+) cells in the areas indicated by boxes in A. Double-immunostaining for GST-pi (green) and lamin B1 (red) reveals that GST-pi (+) cells include both GST-pi (+) C-type cells, which exhibit immunoreactivity for GST-pi in the cytoplasm (B, and arrow in C), and a GST-pi (+) N-type cell, which exhibits immunoreactivity mainly within the nucleus (arrowhead in C). Scale bars=20 μm in (A); 5 μm (B, C).

(30-μm thickness, 0.26 mm to 3.80 mm posterior to bregma) were prepared using a cryostat and collected as free-floating sections.

For detection of BrdU incorporation, brain sections were pre-incubated in 50% formamide/2× saline–sodium citrate buffer for 2 h at 65 °C, incubated in 2 N HCl for 30 min at 37 °C, rinsed in 0.1 M boric acid (pH 8.5) for 10 min at 25 °C, and then washed with 0.3% Triton X-100 in phosphate-buffered saline (PBST), as described previously (Tamura et al., 2004). For multiplex-immunostaining, brain sections were incubated with several primary antibodies at 4 °C for 12–36 h. The primary antibodies used in this study were as follows: monoclonal mouse anti-GST-pi IgG (1:1000, BD Biosciences, San Jose, CA, USA), polyclonal rabbit anti-GST-pi IgG (1:500, Medical and Biological Laboratories, Nagoya, Japan), monoclonal rat anti-BrdU IgG (1:10, Oxford Biotechnology, Oxford, UK), polyclonal rabbit anti-Ki67 IgG (1:1000, NovoCastra, Newcastle, UK), monoclonal mouse anti-NG2 IgG (1:200, Chemicon, Temecula, CA, USA), polyclonal rabbit anti-NG2 IgG (1:200, Chemicon), monoclonal mouse anti-CNPase IgG (1:20,000, Sigma, Taufkirchen, Germany), monoclonal mouse anti-oligodendrocytes (clone RIP) IgG (1:20,000, Chemicon), and polyclonal goat anti-lamin B1 IgG (1:100, Santa Cruz Biotechnology, Santa Cruz, CA, USA). After washing with PBST for 30 min, brain sections were incubated with secondary antibodies conjugated with Cy2, Cy3, or Cy5 (1:200, Jackson ImmunoResearch, West Grove, PA, USA) for 4 h at 4 °C and washed with PBST for 30 min. The sections were mounted with TO-PRO3-containing solution (Molecular Probes, Eugene, OR, USA) and examined using a confocal laser microscope (LSM510META Ver. 3.2; Carl Zeiss, Oberkochen, Germany).

Cell counting procedure

Two brain sections were randomly selected from each animal. The number of cells expressing each oligodendrocyte lineage marker among GST-pi (+) cells was counted in 72 square areas (150 μm×150 μm, 12 square areas in each hemisphere) randomly positioned in layers I–VI of cerebral cortex (motor cortex, M1 and M2; somatosensory cortex, S1BF, S1DZ, S1FL, S1HL, and S1Tr; and auditory cortex, Au1, AuD, and AuV; as defined by Paxinos and Watson, 1998). The number of cells expressing each cellular marker among all BrdU-labeled cells was counted in the same area of each animal. Data from each animal were averaged.

RESULTS

Two subtypes of GST-pi (+) cells

GST-pi (+) cells were widely present throughout layers I–VI of cerebral cortex of adult rats. Double staining for GST-pi and TO-PRO3, a DNA marker, which allows visualization of all cells, especially the nuclei, revealed two different types of GST-pi (+) cells on the basis of intracellular distribution of GST-pi immunoreactivity: cells exhibiting GST-pi immunoreactivity in the cytoplasm (C-type cells, arrows in Fig. 1A) and those exhibiting immunoreactivity in the nucleus (N-type cells, arrowhead in Fig. 1A). In order to visualize the nuclear membrane, immunohistochemical staining for lamin B1, a nuclear envelope protein (Kataoka et al., 2006; Takamori et al., 2007), was performed. Confocal z-series analysis of double-immunofluorescence staining for GST-pi and lamin B1 clearly showed that the C-type cells contained GST-pi mainly in the cytoplasm and little within the nucleus (Fig. 1B and arrow in Fig. 1C), while N-type cells contained this protein mainly in the nucleus and in small amounts in the cytoplasm, especially around the nucleus (arrowhead in Fig. 1C).

Expression of GST-pi in oligodendrocyte-lineage cells

To examine the features of GST-pi (+) C-type and N-type cells in the cerebral cortex, we performed double-immunofluorescence staining using mature oligodendrocyte cell markers (CNPase and RIP). All the cells immunopositive for CNPase were GST-pi (+) cells (arrows in Fig. 2A). However, GST-pi (+) cells without CNPase were also observed (arrowheads in Fig. 2A). Cell counting revealed that 72.6±2.8% (mean±S.D., n=1389 cells from three animals) and 72.4±1.5% (mean±S.D., n=1338 cells from three animals) of GST-pi (+) cells were CNPase (+) and RIP (+), respectively. The distribution of CNPase (+) cells was very similar to that of RIP (+) cells. The antigen recognized with the RIP antibody has recently been iden-

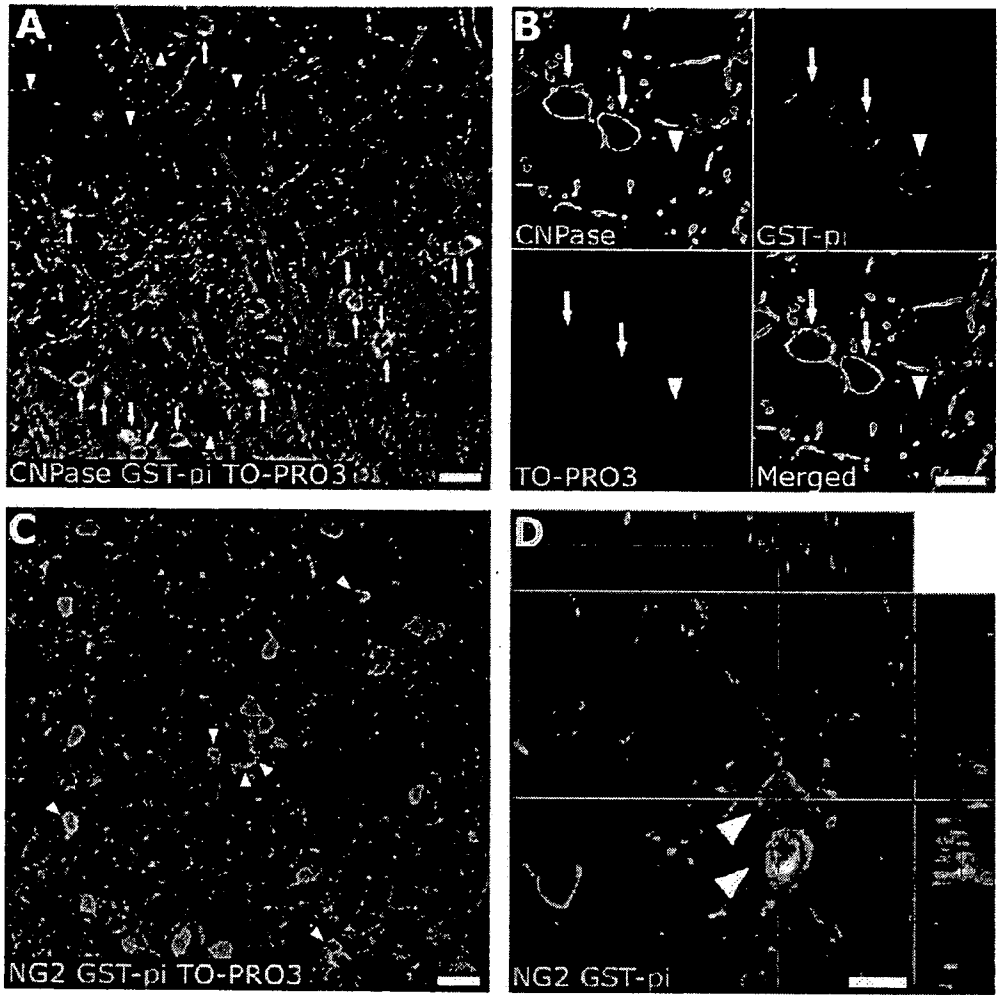

Fig. 2. Phenotypes of GST-pi (+) cells in cerebral cortex. (A, B) Triple staining for CNPase (green), GST-pi (red), and TO-PRO3 (blue) on images of single z-slices. Arrows, GST-pi (+)/CNPase (+) cells; arrowheads, GST-pi (+)/CNPase (−) cells. (C) Triple staining for NG2 (green), GST-pi (red), and TO-PRO3 (blue) on an image of a single z-slice. Arrowheads, GST-pi (+)/NG2 (+) cells. (D) A single-z-slice image with ortho-image of confocal z-stacks (upper and right panels in D) of cells double-labeled (arrowheads) with NG2 (green) and GST-pi (red). Scale bars=20 μm (A, C); 10 μm (B, D).

tified as CNPase (Watanabe et al., 2006). These findings suggested that approximately 70% of GST-pi (+) cells are CNPase (+) and RIP (+) mature oligodendrocytes, while the remaining (approximate 30%) of GST-pi (+) cells were not mature oligodendrocytes. Analysis of the intracellular distribution of GST-pi showed that all GST-pi (+)/CNPase (+) cells and GST-pi (+)/RIP (+) cells were GST-pi (+) C-type cells (arrows in Fig. 2B), whereas a majority of GST-pi (+)/CNPase (−) cells were GST-pi (+) N-type cells (arrowhead in Fig. 2B).

In the adult brain, oligodendrocyte progenitor cells (OPCs) have been identified as NG2-containing cells (Nishiyama et al., 1997; Dawson et al., 2000, 2003). We therefore next performed immunofluorescence staining for GST-pi and NG2 to examine the phenotype of residual GST-pi (+) cells containing neither CNPase nor RIP. In the cortex, all NG2 (+) cells observed in this study were GST-pi (+) cells, and 28.5±2.3% (mean±S.D., n=1384 cells from three animals) of GST-pi (+) cells were immunoreactive for NG2 (arrowheads in Fig. 2C); in addition, 77.2±3.1% (mean±S.D., n=498 cells from three animals) of GST-pi (+)/NG2 (+) cells were GST-pi (+) N-type cells (arrowheads in Fig. 2D) and 22.8±3.1% of them were GST-pi (+) C-type cells. Almost all (99.2±0.1%) GST-pi (+) N-type cells (n=376 cells from three animals) were immunopositive for NG2, while some NG2 (+)/GST-pi (+) N-type cells exhibited very weak immunoreactivity for GST-pi. No clear differences in morphology including cell size and number of processes were noted between NG2 (+)/GST-pi (+) N-type cells and NG2 (+)/GST-pi (+) C-type cells. It was confirmed that neither immunoreactivity for CNPase nor that for RIP was observed in NG2 (+) cells, as previously reported (Keirstead et al., 1998; Dawson et al., 2003).

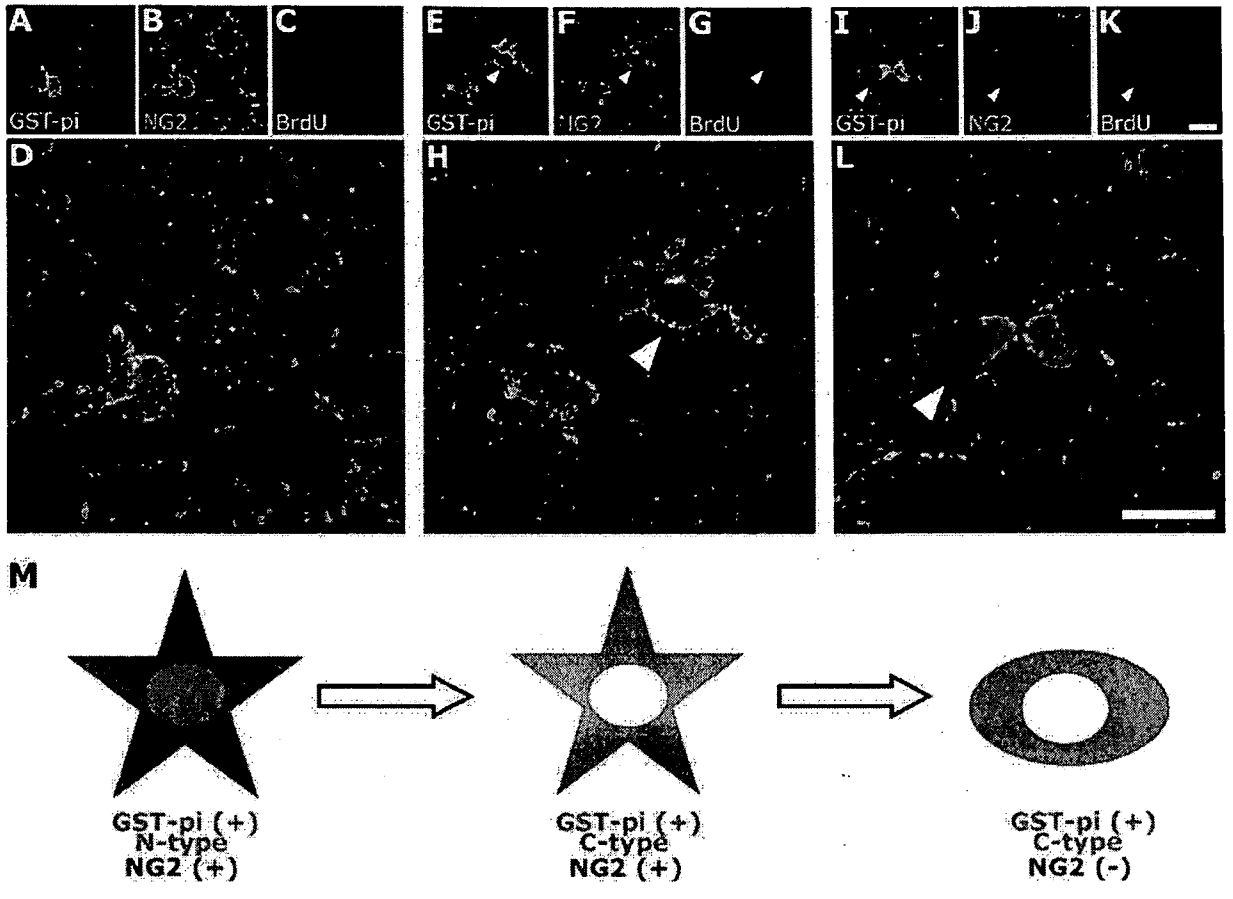

Fig. 3. GST-pi (+) N-type oligodendrocyte progenitor cells differentiated into GST-pi (+) C-type mature oligodendrocytes. (A–L) Triple immunolabeling for GST-pi (green), NG2 (red), and BrdU (blue) on images of single z-slices. An NG2 (+)/GST-pi (+) N-type BrdU-labeled cell at 2 h after BrdU injection (A–D). An NG2 (+)/GST-pi (+) N-type BrdU-labeled cell and an NG2 (+)/GST-pi (+) C-type BrdU-labeled cell (arrowheads) at 14 days after BrdU injection (E–H). An NG2 (−)/GST-pi (+) C-type BrdU-labeled cell at 28 days after BrdU injection (arrowheads in I–L). A–C, E–G, and I–K are at the same magnification; scale bar=10 μm (K). D, H, and L are at the same magnification; scale bar=10 μm (L). (M) Schema of pattern of immunoreactivity for GST-pi (green) and NG2 (red) in oligodendrocyte-lineage cells.

Nuclear GST-pi (+) (N-type) cells differentiate into cytoplasmic GST-pi (+) (C-type) cells

To determine whether GST-pi (+) N-type cells differentiate into GST-pi (+) C-type mature oligodendrocytes *in vivo*, triple-immunofluorescence staining for BrdU, GST-pi, and NG2 was performed using brain sections taken at several time points after a single injection of BrdU. At 2 h after BrdU injection, 94.7±1.9% of BrdU-labeled cells (mean± S.D., n=134 cells from three animals) were NG2 (+)/ GST-pi (+) N-type cells (Fig. 3A–D). Almost all Ki67 (+) cells corresponded to GST-pi (+) N-type cells (data not shown), indicating that these cells were the major proliferating cell population. At 14 days after injection, in addition to BrdU-labeled NG2 (+)/GST-pi (+) N-type cells (82.8±4.6%; mean±S.D., n=201 cells from three animals), 9.7±2.0% (mean±S.D., n=201 cells from three animals) of BrdU-labeled cells were NG2 (+)/GST-pi (+) C-type cells (arrowheads in Fig. 3E–H). However, no NG2 (−)/GST-pi (+) C-type cells were observed among BrdU-labeled cells. These findings suggest that NG2 (+)/GST-pi (+) C-type cells are at the intermediate-differentiation stage in the oligodendrocyte lineage. At 28 days after injection, in addition to BrdU-labeled NG2 (+)/GST-pi (+) N-type cells (74.0±4.0% of BrdU-labeled cells, mean± S.D., n=227 cells from three animals) and NG2 (+)/ GST-pi (+) C-type cells (11.8±2.0% of BrdU-labeled cells, mean±S.D., n=227 cells from three animals), 8.5±1.2% of BrdU-labeled cells (mean±S.D., n=227 cells from three animals) were NG2 (−)/GST-pi (+) C-type cells (arrowheads in Fig. 3I–L). These findings indicate that GST-pi (+) N-type cells differentiate into GST-pi (+) C-type mature oligodendrocytes.

DISCUSSION

It has been reported that GST-pi is expressed in carbonic anhydrase- or CNPase-positive mature oligodendrocytes in the adult rodent brain (Cammer et al., 1989; Tansey and Cammer, 1991). In the present study, we found, in the cerebral cortex of adult rats, that approximately 70% of GST-pi (+) cells were CNPase (+) and RIP (+) mature oligodendrocytes (Fig. 2A and B), while the residual 30% were NG2 (+) oligodendrocyte progenitor cells expressing

neither CNPase nor RIP (Fig. 2B and C). Although GST-pi has been used as a specific marker protein for identification of mature oligodendrocytes (Tanaka et al., 2003; Mason et al., 2004; Gotts and Chesselet, 2005), our findings indicate that careful usage of it will be necessary.

We demonstrated that two types of GST-pi (+) cells exhibited different subcellular localizations of GST-pi protein; mature oligodendrocytes contained GST-pi protein mainly in the cytoplasm (C-type cells) (Fig. 1B and arrow in Fig. 1C), while progenitor cells contained the protein mainly within the nucleus (N-type cells) (arrowhead in Fig. 1C). Even on confocal laser microscopy, it was occasionally difficult to distinguish between the N-type and C-type cells at low magnification (Fig. 2C). However, use of the profile mode of confocal laser microscope software at high magnification permitted identification of such cell types on the basis of fluorescence intensity.

These findings were demonstrated by immunohistochemical studies with both monoclonal and polyclonal anti-GST-pi antibodies. Furthermore, we confirmed by Western blotting that both monoclonal and polyclonal antibodies recognized only 23 kDa GST-pi protein in tissue homogenates from cerebral cortex of adult rats (data not shown).

In the BrdU-labeling study, almost all BrdU-labeled cells were NG2 (+)/GST-pi (+) N-type cells at 2 h after BrdU injection (Fig. 3A–D). At 14 days after injection, NG2 (+)/GST-pi (+) C-type cells began to appear besides NG2 (+)/GST-pi (+) N-type cells among BrdU-labeled cells (arrowheads in Fig. 3E–H). At 28 days after injection, NG2 (−)/GST-pi (+) C-type cells could be observed among BrdU-labeled cells in addition to the types of cells observed at 14 days (arrowheads in Fig. 3I–L). These findings indicate that NG2 (+)/GST-pi (+) N-type cells differentiate into mature oligodendrocytes, which are NG2 (−)/GST-pi (+) C-type cells, through intermediate cells, which are NG2 (+)/GST-pi (+) C-type cells (Fig. 3M).

Nuclear expression of GST-pi has been reported in human uterine cancer (Shiratori et al., 1987), human metastatic neuroblastoma (Hall et al., 1994), and human glioma (Ali-Osman et al., 1997). These observations suggest that nuclear GST-pi expression is related to cellular proliferation. Indeed, in the present study, only NG2 (+)/GST-pi (+) N-type cells exhibited proliferative activity among GST-pi (+) cells in adult cortex (Fig. 3A–D). Although the functional significance of translocation of GST-pi protein from the cell nucleus to the cytoplasm remains to be determined, observation of the intracellular location of these markers permits identification of the stages of differentiation of oligodendrocyte lineage cells.

Acknowledgments—This work was supported in part by Special Coordination Funds for Promoting Science and Technology from the Ministry of Education, Culture, Sports, Science, and Technology, Japan, to Y.K., by consignment expenses from the Molecular Imaging Program on "Research Base for Exploring New Drugs" from the Ministry of Education, Culture, Sports, Science, and Technology to Y.W., and by a Grant-in-Aid for Scientific Research (No. 16590157) from the Japan Society for Promotion of Science to H.Y.

REFERENCES

Abramovitz M, Homma H, Ishigaki S, Tansey F, Cammer W, Listowsky I (1988) Characterization and localization of glutathione-S-transferases in rat brain and binding of hormones, neurotransmitters, and drugs. J Neurochem 50:50–57.

Abramovitz M, Listowsky I (1987) Selective expression of a unique glutathione S-transferase Yb3 gene in rat brain. J Biol Chem 262:7770–7773.

Ali-Osman F, Brunner JM, Kutluk TM, Hess K (1997) Prognostic significance of glutathione S-transferase pi expression and subcellular localization in human gliomas. Clin Cancer Res 3:2253–2261.

Board PG, Baker RT, Chelvanayagam G, Jermiin LS (1997) Zeta, a novel class of glutathione transferases in a range of species from plants to humans. Biochem J 328(Pt 3):929–935.

Board PG, Coggan M, Chelvanayagam G, Easteal S, Jermiin LS, Schulte GK, Danley DE, Hoth LR, Griffor MC, Kamath AV, Rosner MH, Chrunyk BA, Perregaux DE, Gabel CA, Geoghegan KF, Pandit J (2000) Identification, characterization, and crystal structure of the omega class glutathione transferases. J Biol Chem 275: 24798–24806.

Cammer W, Tansey F, Abramovitz M, Ishigaki S, Listowsky I (1989) Differential localization of glutathione-S-transferase Yp and Yb subunits in oligodendrocytes and astrocytes of rat brain. J Neurochem 52:876–883.

Cammer W, Zhang H (1992) Localization of Pi class glutathione-S-transferase in the forebrains of neonatal and young rats: evidence for separation of astrocytic and oligodendrocytic lineages. J Comp Neurol 321:40–45.

Dawson MR, Levine JM, Reynolds R (2000) NG2-expressing cells in the central nervous system: are they oligodendroglial progenitors? J Neurosci Res 61:471–479.

Dawson MR, Polito A, Levine JM, Reynolds R (2003) NG2-expressing glial progenitor cells: an abundant and widespread population of cycling cells in the adult rat CNS. Mol Cell Neurosci 24:476–488.

Gotts JE, Chesselet MF (2005) Migration and fate of newly born cells after focal cortical ischemia in adult rats. J Neurosci Res 80:160–171.

Hall AG, McGuckin AG, Pearson AD, Cattan AR, Malcolm AJ, Reid MM (1994) Glutathione S-transferase in bone marrow metastases of disseminated neuroblastoma. J Clin Pathol 47:468–469.

Johnson JA, El Barbary A, Kornguth SE, Brugge JF, Siegel FL (1993) Glutathione S-transferase isoenzymes in rat brain neurons and glia. J Neurosci 13:2013–2023.

Kataoka Y, Tamura Y, Takamori Y, Cui Y, Yamada H (2006) Perineuronal germinal cells in the rat cerebral cortex. Med Mol Morphol 39:28–32.

Keirstead HS, Levine JM, Blakemore WF (1998) Response of the oligodendrocyte progenitor cell population (defined by NG2 labelling) to demyelination of the adult spinal cord. Glia 22:161–170.

Li NQ, Reddanna P, Thyagaraju K, Reddy CC, Tu CP (1986) Expression of glutathione S-transferases in rat brains. J Biol Chem 261:7596–7599.

Mannervik B, Alin P, Guthenberg C, Jensson H, Tahir MK, Warholm M, Jornvall H (1985) Identification of three classes of cytosolic glutathione transferase common to several mammalian species: correlation between structural data and enzymatic properties. Proc Natl Acad Sci U S A 82:7202–7206.

Mason JL, Toews A, Hostettler JD, Morell P, Suzuki K, Goldman JE, Matsushima GK (2004) Oligodendrocytes and progenitors become progressively depleted within chronically demyelinated lesions. Am J Pathol 164:1673–1682.

Meyer DJ, Coles B, Pemble SE, Gilmore KS, Fraser GM, Ketterer B (1991) Theta, a new class of glutathione transferases purified from rat and man. Biochem J 274(Pt 2):409–414.

Meyer DJ, Thomas M (1995) Characterization of rat spleen prostaglandin H D-isomerase as a sigma-class GSH transferase. Biochem J 311(Pt 3):739–742.

Nishiyama A, Yu M, Drazba JA, Tuohy VK (1997) Normal and reactive NG2+ glial cells are distinct from resting and activated microglia. J Neurosci Res 48:299–312.

Paxinos G, Watson C (1998) The rat brain in stereotaxic coordinates, 4th ed. San Diego: Academic Press.

Pemble SE, Wardle AF, Taylor JB (1996) Glutathione S-transferase class kappa: characterization by the cloning of rat mitochondrial GST and identification of a human homologue. Biochem J 319(Pt 3):749–754.

Shiratori Y, Soma Y, Maruyama H, Sato S, Takano A, Sato K (1987) Immunohistochemical detection of the placental form of glutathione S-transferase in dysplastic and neoplastic human uterine cervix lesions. Cancer Res 47:6806–6809.

Takamori Y, Tamura Y, Kataoka Y, Cui Y, Seo S, Kanazawa T, Kurokawa K, Yamada H (2007) Differential expression of nuclear lamin, the major component of nuclear lamina, during neurogenesis in two germinal regions of adult rat brain. Eur J Neurosci 25:1653–1662.

Tamura Y, Kataoka Y, Cui Y, Yamada H (2004) Cellular proliferation in the cerebral cortex following neural excitation in rats. Neurosci Res 50:129–133.

Tanaka K, Nogawa S, Suzuki S, Dembo T, Kosakai A (2003) Upregulation of oligodendrocyte progenitor cells associated with restoration of mature oligodendrocytes and myelination in peri-infarct area in the rat brain. Brain Res 989:172–179.

Tansey FA, Cammer W (1991) A pi form of glutathione-S-transferase is a myelin- and oligodendrocyte-associated enzyme in mouse brain. J Neurochem 57:95–102.

Terrier P, Townsend AJ, Coindre JM, Triche TJ, Cowan KH (1990) An immunohistochemical study of pi class glutathione S-transferase expression in normal human tissue. Am J Pathol 137: 845–853.

Theodore C, Singh SV, Hong TD, Awasthi YC (1985) Glutathione S-transferases of human brain. Evidence for two immunologically distinct types of 26500-Mr subunits. Biochem J 225:375–382.

Watanabe M, Sakurai Y, Ichinose T, Aikawa Y, Kotani M, Itoh K (2006) Monoclonal antibody Rip specifically recognizes 2′,3′-cyclic nucleotide 3′-phosphodiesterase in oligodendrocytes. J Neurosci Res 84:525–533.

(Accepted 13 June 2007)
(Available online 2 August 2007)

Available online at www.sciencedirect.com
ScienceDirect
ELSEVIER
Nuclear Instruments and Methods in Physics Research A 580 (2007) 1363–1371
NUCLEAR INSTRUMENTS & METHODS IN PHYSICS RESEARCH Section A
www.elsevier.com/locate/nima

Development of a low-noise analog front-end ASIC for CdTe detectors

Tetsuichi Kishishita[a,b,*], Hirokazu Ikeda[a], Tatsuya Kiyuna[c], Ken-ichi Tamura[a,b], Kazuhiro Nakazawa[b], Tadayuki Takahashi[a,b]

[a]*Institute of Space and Astronautical Science, Japan Aerospace Exploration Agency, Sagamihara, Kanagawa 229-8510, Japan*
[b]*Department of Physics, The University of Tokyo, Bunkyo, Tokyo 113-0033, Japan*
[c]*Acrorad Co., Ltd., Uruma, Okinawa 904-2234, Japan*

Received 1 May 2007; received in revised form 11 June 2007; accepted 3 July 2007
Available online 13 July 2007

Abstract

This paper describes the recent development of a low-noise analog front-end ASIC for CdTe detectors. The ASIC is designed on the basis of the Open-IP LSI project led by JAXA and implemented using TSMC 0.35-μm CMOS technology. The ASIC contains eight identical channels, each of which includes a charge-sensitive amplifier, band-pass filters, and a sample-and-hold circuit. Preliminary testing of the ASIC achieved noise performance of $188e^- + 7.5e^-/pF$. In order to verify the low-noise characteristics, the ASIC was connected to a guard-ring-equipped CdTe diode detector with dimensions of 2.4 × 2.4 mm and having a thickness of 0.5 mm. As a result, the gamma-ray spectra of radioactive sources were obtained with good energy resolutions of 2.51 and 2.35 keV (FWHM) for gamma rays of 59.5 and 122 keV, respectively, at room temperature.

PACS: 29.30.Kv

Keywords: ASIC; Open-IP; Low noise; X-ray; Gamma ray; CdTe; Analog front-end

1. Introduction

One of the primary objectives of future X-ray missions is to explore the universe with very high sensitivity in the 10–100 keV band, where nonthermal emission becomes dominant over thermal emission. This exploration could be achieved by employing a multilayer, grazing incidence hard X-ray telescope ("super mirror") in conjunction with a hard X-ray imaging detector used as a focal plane detector [1–3]. The detector system would require a high energy resolution of better than 1 keV (Full-Width-at-Half-Maximum or FWHM) at 60 keV and a spatial resolution of better than 200 μm. Cadmium telluride (CdTe) has been considered a promising semiconductor material for focal detector systems, given its high stopping power of X-rays and gamma rays. Significant progress has been made in crystal growth technology to enable the development of large-area detectors, with good energy resolutions being reported in combination with several low-noise ASICs [4–8].

In the past few years, we have been working on the development of low-noise analog ASICs for gamma-ray detectors; specifically, one-dimensional ASICs [9] and two-dimensional ASICs [10]. The one-dimensional ASICs have relatively simple circuits and the main objective is to construct a set of verified designs of circuit blocks to be used for signal processing in radiation detectors. Conversely, the two-dimensional ASICs were developed for the hybrid pixel imaging detector to be used in the hard X-ray and gamma-ray observations in space. Both ASICs have reached a noise level of less than $300e^-$, although practical use requires further improvement of noise performance.

To achieve ASICs of even lower noise, we have newly developed a one-dimensional, eight-channel, low-noise analog ASIC designated the "KW01". The main objective

*Corresponding author. Institute of Space and Astronautical Science, Japan Aerospace Exploration Agency, Sagamihara, Kanagawa 229-8510, Japan.
E-mail address: kisisita@astro.isas.jaxa.jp (T. Kishishita).

0168-9002/$ - see front matter © 2007 Elsevier B.V. All rights reserved.
doi:10.1016/j.nima.2007.07.003

here is to demonstrate the newly designed circuit blocks and establish a low-noise architecture. All circuit architectures are based on the Open-IP LSI project led by JAXA [9–11]. Since Open-IP consists of reusable circuit blocks extracted from our ASIC designs, the circuit library is flexibly updated with and applicable to the further development of low-noise two-dimensional ASICs.

This paper presents the design and initial performance of the KW01 chip. Section 2 describes the basic structure of the KW01 and details the circuit schematics. The ASIC employs a newly designed high-impedance circuit instead of an FET used as a transfer gate for a feedback component, as is often used in several low-noise ASICs [12–18]. Section 3 presents the setup of the performance measurements. Section 4 gives the preliminary experimental results of ASIC performance. Section 5 reports on the spectral performance in combination with a CdTe diode detector. Finally, Section 6 gives a summary and conclusion.

2. Circuit description

2.1. Overview of the ASIC

The KW01 is implemented using TSMC 0.35-μm CMOS technology with such options as 4-metal, 2-poly, and mounted in a plastic-mold package. Fig. 1 shows a photograph of the ASIC. The chip size is 2.95 × 2.95 mm with eight readout channels, and has total power consumption of 33 mW for the power rails of ±1.65 V. There exists some penalty on the power consumption to improve the dynamic range. The buffer circuits equipped for monitoring analog signals also contribute additional power dissipation. In order to mitigate interference between the analog and digital circuits, special care was taken for the layout as follows: (a) the area surrounding the entire chip is separated between the analog and digital circuits, (b) the digital circuits are concentrated on the right side of the chip and analog signals are processed in the left-to-right direction, and (c) bias and reference voltages are supplied from the top and bottom sides of the chip. Table 1 lists an overview of the ASIC.

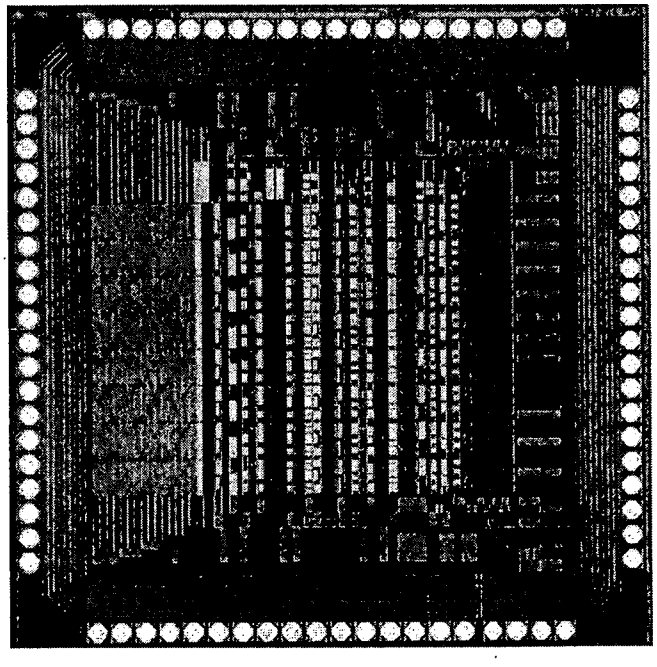

Fig. 1. Photograph of the KW01. Pads on the right and the bottom-right sides are for the digital circuits, and the others for analog circuits. Inputs for injected charge are on the left, with analog signals processed in the left-to-right direction. Output and monitor pads are on the top side. Bias voltages are supplied from both the top and bottom pads.

2.2. Analog processing

The analog circuit chain consists of a charge-sensitive amplifier (CSA), band-pass filters, comparator, and sample-and-hold circuit as shown in Fig. 2. CSA input is provided with an ESD protection circuit. A capacitor ($C_{in} = 0.1$ pF) is attached for test pulse injection. CSA output is split into two different filter circuits whose circuit architectures are identical except for the time constants. The faster circuit (with a peaking time of 1.5 μs) is fed into the comparator to generate a hit signal with an one-shot trigger circuit. The slower circuit (with a peaking time of 3 μs) is connected to the sample-and-hold circuit with a storage capacitor of $C_h = 0.8$ pF. Analog outputs for the eight readout channels are held simultaneously by a properly timed external signal and serially read out in a multiplexing scheme.

The transfer function of the CSA is given as

$$T_1(s) = -\frac{R_f}{1 + sC_fR_f} \tag{1}$$

where s denotes the complex angular frequency, R_f the feedback resistance, and C_f the feedback capacitance.

In order to focus on the basic properties of the circuit chain in the present ASIC, a pole-zero-cancellation circuit is not employed. Instead, we adopted a large decay-time constant of C_fR_f for the CSA and attempted to reduce the undershoot as well as decrease the contribution of shot noise.

Fig. 2 shows the filter circuit as a rectangle of dashed lines. The transfer function of the filter circuit is given as

$$T_2(s) = -\frac{sC_0R_1}{s^2C_1C_2R_1R_2 + sR_1C_1 + 1}. \tag{2}$$

Table 1
Overview of the KW01

Fabrication process	TSMC 0.35-μm CMOS
Options	4-metal, 2-poly
Chip size	2.95 × 2.95 mm^2
Number of channels	8
Total power consumption	33 mW
Power rail	±1.65 V

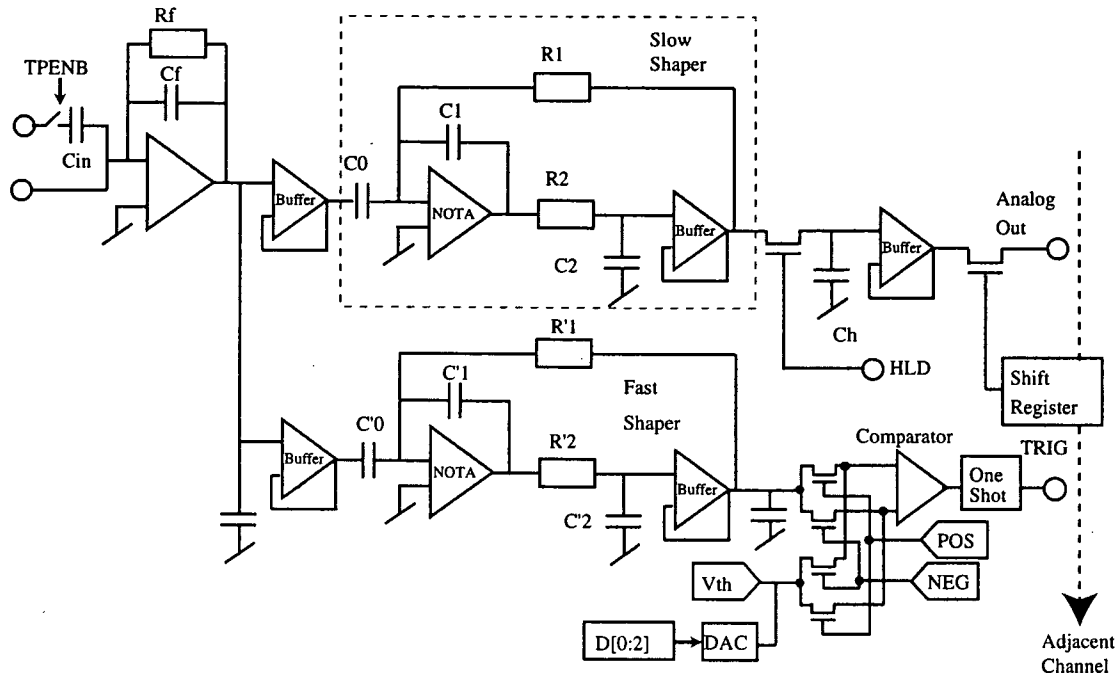

Fig. 2. Signal processing chain for each channel. Here, typical values of the capacitors and resistors are $C_{in} = 0.1$ pF, $R_f = 400$ MΩ, $C_f = 0.02/0.04$ pF, $C_0 = 3.2/6.4$ pF, $C_1 = C_2 = 0.5/1.0$ pF, $R_1 = R'_1 = 6$ MΩ, $C'_0 = 0.66/1.32$ pF, $C'_1 = C'_2 = 0.1/0.2$ pF, $R_2 = R'_2 = 1.5$ MΩ, $C_h = 0.8$ pF.

By setting the parameters as $C_1R_1 = 4C_2R_2$, the transfer function is reduced as

$$-\frac{sC_0R_1}{(2sC_2R_2+1)^2}. \tag{3}$$

This circuit has a degenerated pole at $s = -1/2C_2R_2$ and functions as a low-pass filter. Eventually the entire transfer function of the signal processing chain is given by $T_1(s) \cdot T_2(s)$, which yields

$$\frac{R_f}{1+sC_fR_f} \cdot \frac{sC_0R_1}{(2sC_2R_2+1)^2}. \tag{4}$$

By assuming $C_fR_f \gg 1/|s|$, the zero of $T_2(s)$ compensates the pole of $T_1(s)$ and the transfer function is rewritten as

$$2 \cdot \frac{C_0}{C_f \cdot C_1} \cdot \frac{1/T_M}{(s+1/T_M)^2} \tag{5}$$

where we employ the relation $T_M = 2C_2R_2$. In case C_fR_f is not negligible compared to T_M, the transfer function is given as

$$2 \cdot \frac{C_0}{C_f \cdot C_1} \cdot \frac{1/T_M}{(s+1/T_M)^2} \cdot \frac{s}{(s+1/C_fR_f)}. \tag{6}$$

Should this be the case unlike in Eq. (5), undershoot occurs, although a high count rate is not required in space applications. Thus, the degradation of pulse height is thought to be sufficiently small.

As for the case of Eq. (5), the entire circuit functions as a CR-RC shaper and the equivalent noise charge is written as follows [19]:

$$Q_n^2 = \left(\frac{e^2}{8}\right)\left[\left(2qI_d + \frac{4kT}{R_p}\right) \cdot T_M + (4kTR_S) \cdot \frac{C_D^2}{T_M} + 4A_fC_D^2\right] \tag{7}$$

where q denotes the electronic charge, k the Boltzmann constant, T the absolute temperature, I_d the detector leakage current, R_p the input shunt resistance located in parallel with the detector capacitance C_D, T_M the peaking time of the shaper, R_S ($= 2/3g_m$ in the simplest presentation) the resistance equivalently located in series to the preamplifier input, and A_f the coefficient of the $1/f$ noise component.

2.3. Charge-sensitive amplifier

Fig. 3 shows the detailed CMOS circuit configuration of the CSA. The CSA consists of a preamplifier, feedback circuit, and feedback capacitor C_f. The amplifier part consists of a folded cascode amplifier with a gain boost for the cascode transistor. Table 2 lists the dimensions of the PMOS input transistor and the main characteristics of the CSA. The feedback circuit consists of four p-channel transistors operated in a weak-inversion mode where the source drain current is linear with respect to the difference between the gate voltages of M2 and M5 (in Fig. 3). The impedance is equivalent to the total transconductance of M2 to M5 and the effective impedance of R_f is about 400 MΩ. These circuit blocks were commonly employed in

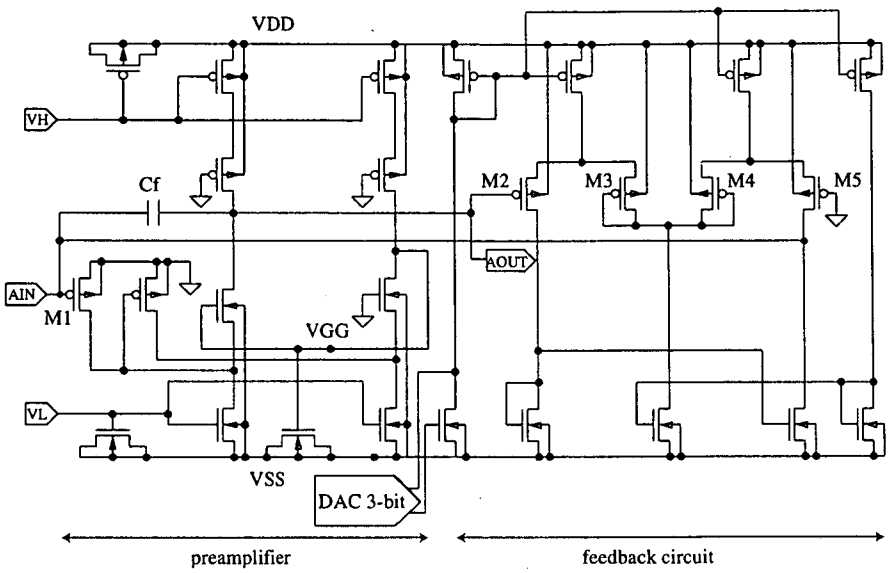

Fig. 3. Detailed schematic of the charge-sensitive amplifier.

Table 2
Parameters for the charge-sensitive amplifier

Main characteristics	PMOS input, gain-boost for cascode
Input transistor dimensions (W/L/M)	1440 μm/1.8 μm/180
Transconductance (g_m)	1.73 mS with $I_d = 107\,\mu A$
Effective impedance of feedback circuit (R_f)	$\simeq 400\,M\Omega$
Feedback capacitance (C_f)	0.02/0.04 pF

previous ASICs [9,10]. Feedback capacitor C_f can be selected among 0.02 and 0.04 pF.

2.4. High-resistance circuit

Fig. 4 shows a detailed schematic of the high-resistance circuit. Current I_R flows into a 20-kΩ resistor R according to the difference in voltage between nodes VIN and IOUT. Assuming matching among the geometrically identical MOS devices, I_R is divided between M1 and M2, or M3 and M4. The drain currents of M1 and M4 are given as $\frac{1}{5} \times I_R$, while those of M2 and M3 as $\frac{4}{5} \times I_R$. This partitioning factor is determined by the M value, which indicates the number of FET gates arranged in parallel. The following current mirrors of M5 to M6 and M7 to M8 set the output current at $\frac{1}{100} \times I_R$ at node IOUT. As a result, the overall circuit virtually boosts the impedance value of resistor R by an attenuation factor of 100, and thus functions as a 2-MΩ resistor. The reference current supplied from outside the chip is attenuated in the bias circuit and then applied to the high-resistance circuit as constant current sources (M9 and M10). Fig. 5 shows simulated frequency characteristics of the high-resistance circuit as obtained through circuit simulation. Eventually the effective impedances of R_2 and R_2' in Fig. 2 are about 1.5 MΩ (with an attenuation factor of 100), while those of R_1 and R_1' are about 6 MΩ (with an attenuation factor of 400).

2.5. Control scheme

Each channel contains a 15-bit configuration register. Three bits are used for switching the decay-time constant of the CSA, six bits for baseline equalization (three bits per filter circuit), three bits for threshold equalization, one bit for masking noisy channels, one bit for selecting the polarity of input signals, and one bit to enable the test input pulse. In addition, a five-bit central register is equipped to provide common settings among the channels. Two bits are used for selecting monitor output among the CSA and slow and fast filters, two bits for switching the peaking time of the filter circuits (one bit per filter circuit), and one bit for selecting the preamplifier gain ($C_f = 0.02$ or 0.04 pF). All bits are stores in D-type flip-flops.

3. Setup of performance measurements

In the experimental setup, the ASIC is held in a QFP-80 socket mounted on the test board. The test board is also placed in a light-shielded aluminum box. The interface with a computer is established using a National Instruments PCI-7833R board that contains a reconfigurable FPGA.

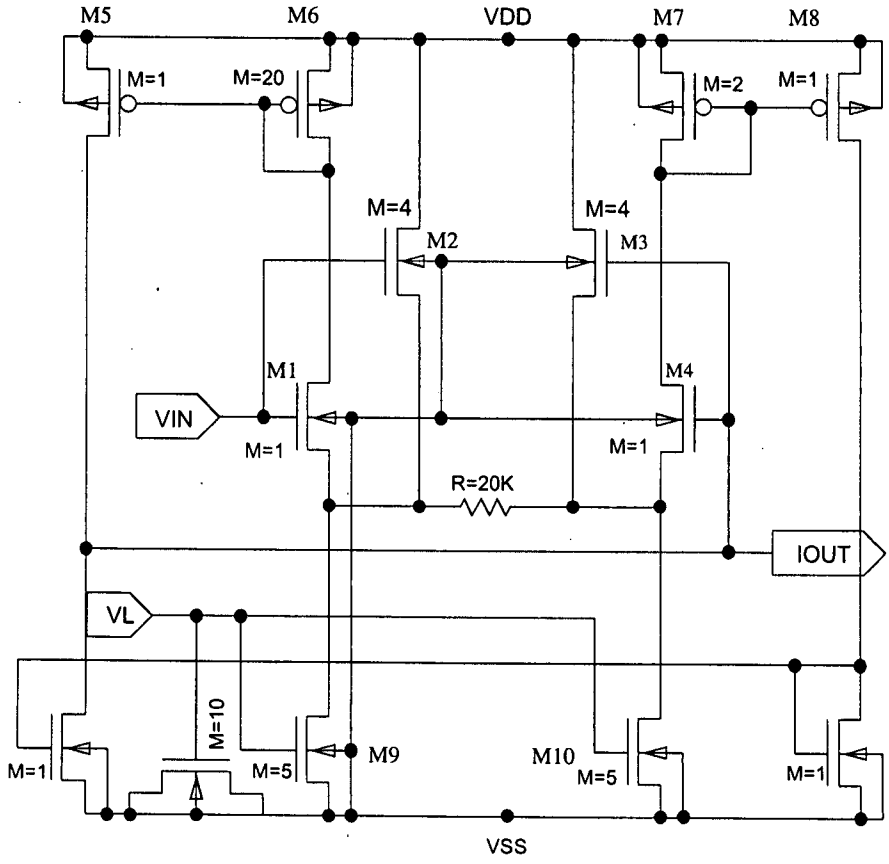

Fig. 4. Detailed schematic of the high-resistance circuit.

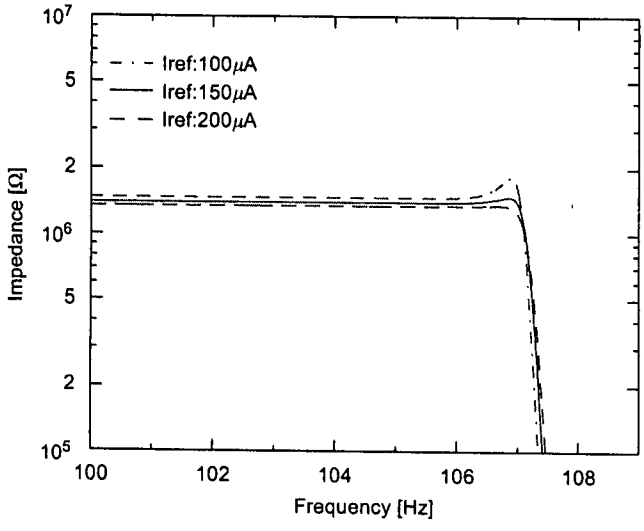

Fig. 5. Frequency characteristics of the high-resistance circuit with SPICE simulation. I_{ref} is a reference current supplied to a bias circuit connected to the resistance circuit.

LabView software tools were used to control the readout sequence. The interface signals are organized into three groups: CMOS inputs, LVDS inputs, and LVDS outputs. Since CMOS signals for the KW01 are operated with $V_{DD} = 1.65\,V$ and $V_{SS} = -1.65\,V$, the signals must be converted from or into LVTTL signals for the PCI-7833R board. Given the typical offset voltage of 1 V for commercial LVDS drivers, their outputs are leveled down in DC by 1 V before being fed into the chip. In order to mitigate interference with an analog processing chain, we chose LVDS for the trigger and hold signals.

4. Experimental results

4.1. Waveform of analog output

Fig. 6 shows the measured waveform traces of analog outputs with both positive and negative input charges of 2 fC. All measurements were performed in high gain mode (where $C_f = 0.02\,pF$). Although the peaking times are longer than in the simulation, the negative ones are closer to the design value. The pulse heights are consistent with the simulation results. As shown in the upper panel in Fig. 6, note that the undershoot or overshoot is not excessive even without a pole-zero-cancellation circuit. In the case of $T_M = 3\,\mu s$, $C_f R_f$ ($= 8\,\mu s$) is not negligible compared with T_M and the undershoot is shown somewhat in the lower panel of Fig. 6. However, our application required no high count rate.

4.2. Linearity

Fig. 7 shows the linearity curves of a typical channel. The configuration settings are the same for both negative and positive input signals. As this figure shows, the linearity curves are consistent with the simulation results until a maximum output swing of about 1 V.

The lower panel of Fig. 7 shows the residuals between the measured data points and linear functions. Note that different linear functions are used for calculating the residuals between positive and negative polarities. The linearity curve between −4 and +3.5 fC is maintained with an integral nonlinearity of 5% in high gain mode ($C_f = 0.02$ pF), while that between −10 and +7 fC in low gain mode ($C_f = 0.04$ pF).

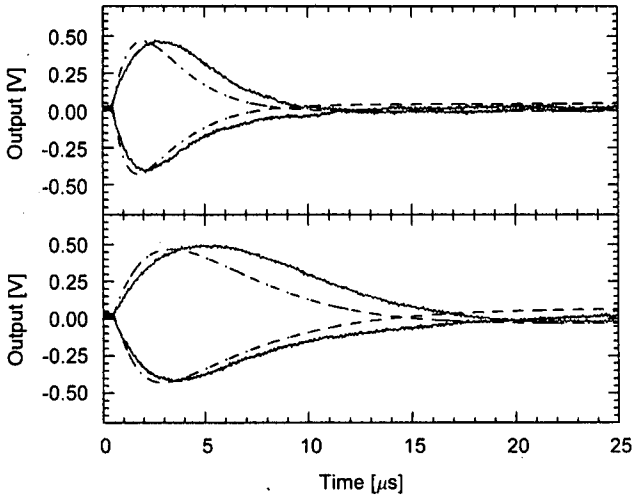

Fig. 6. Measured analog waveforms of a typical channel together with simulation data points (dot-dash line). The upper panel shows the data for $T_M = 1.5\,\mu s$ mode and the lower for $T_M = 3\,\mu s$ mode. The injected test pulse is 2 fC.

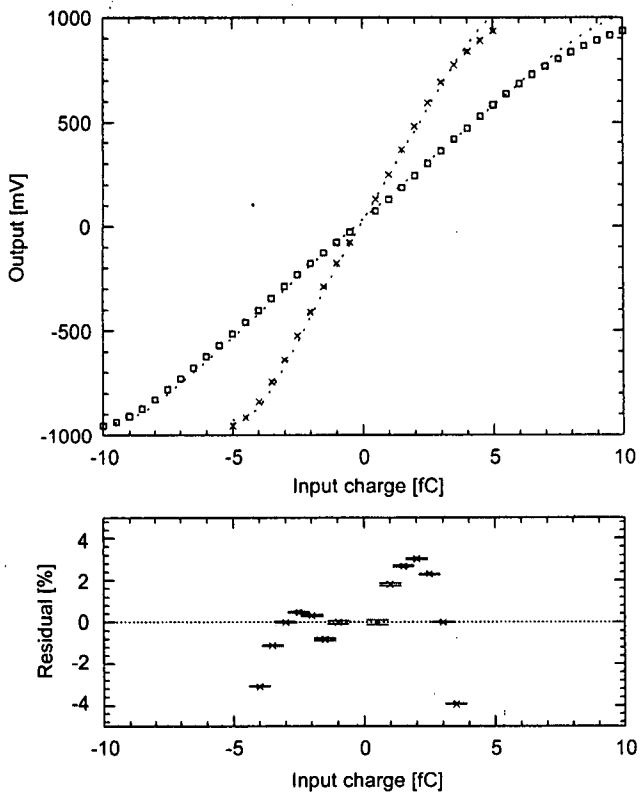

Fig. 7. Linearity curve of a typical channel. The measured data points are shown together with the simulation results (dotted line). The circles are the data points for $C_f = 0.04$ pF and squares for $C_f = 0.02$ pF. The lower plots indicate the residuals between data points and linear functions.

4.3. Noise performance

Fig. 8 shows the measured noise performance. The rms noise is $188e^- + 7.5e^-/pF$ for a peaking time of 3 μs and $205e^- + 10.6e^-/pF$ for a peaking time of 1.5 μs. Although the noise slopes are nearly consistent with the simulation results, the curves have an excess of $210e^-$. The origin of that excess is being investigated. The measurements were performed with the ASIC in a plastic-mold package mounted on a burn-in socket, and thus the intrinsic noise level is expected to be lower than the measured value. The theoretically expected noise level is $48e^-$ at input capacitance of 0 pF.

4.4. Channel-to-channel variations in analog performance

The other aspects of analog performance were evaluated for 10 chips (a total of 80 channels). Table 3 summarizes the measurements.

Fig. 9 shows the distribution of the CSA baseline. We found that 11 channels strayed too far from ground level and did deliver analog outputs. This phenomenon is probably due to excessively large leakage current of the

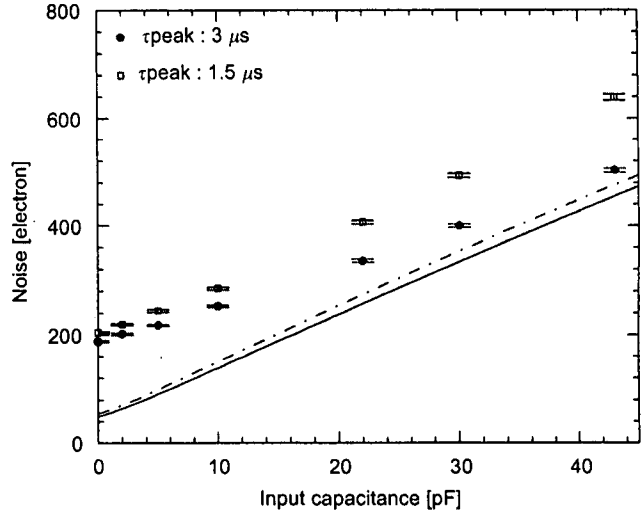

Fig. 8. Input capacitance versus noise level (ENC). The solid and dot-dash lines show results from a circuit simulation, and the circles and squares are the measured data points.

Table 3
Summary of analog performance

Gain	205 mV/fC for $C_f = 0.02$ pF, 112 mV/fC for $C_f = 0.04$ pF
Gain variation	5.5%
Noise level	$188e^- + 7.5e^-$/pF (rms)
Peaking time	3.93 or 1.95 μs
Peaking time variation (σ)	6.1% chip-to-chip

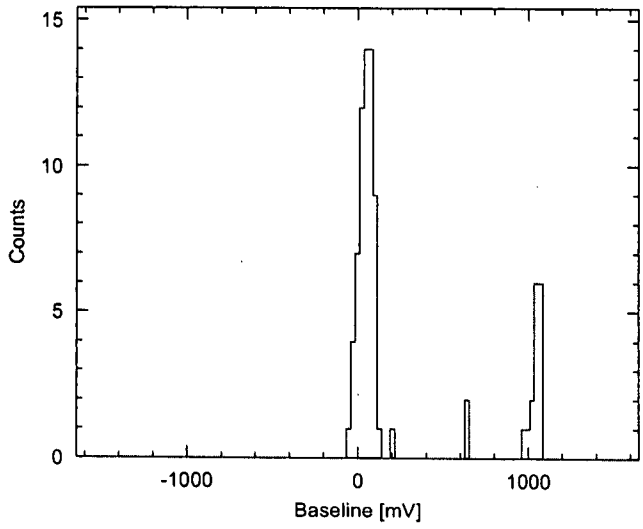

Fig. 9. Baseline distribution of the CSA.

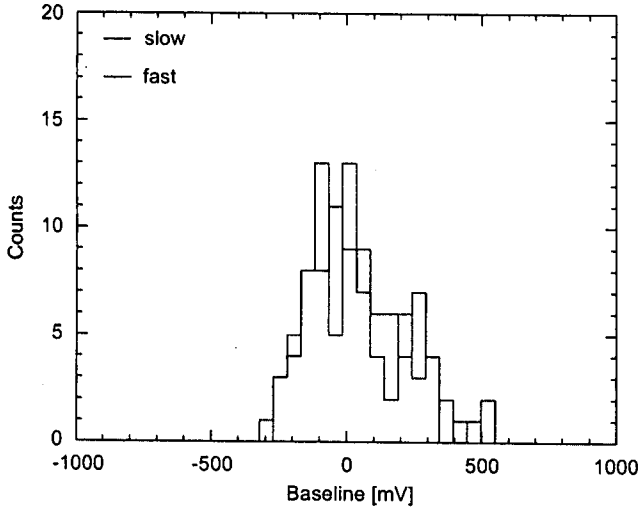

Fig. 10. Baseline distribution before adjustment.

ESD protection circuit in competing with the feedback current of the CSA. To resolve this problem, a leakage current compensation circuit will be employed in the next ASIC.

Figs. 10 and 11 show the baseline distribution before and after adjusting the offset DACs, respectively. The baseline distributions of the slow and fast filters without adjustment are 19 ± 169 and 6 ± 183 mV, respectively. Applying the

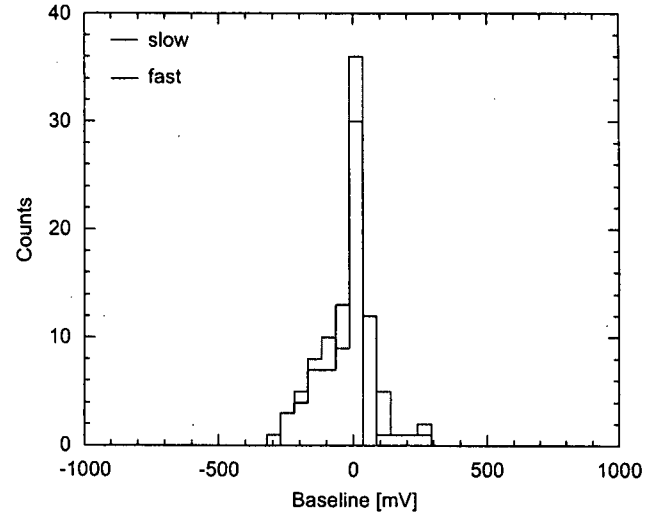

Fig. 11. Baseline distribution after adjustment.

baseline adjustment improves the distributions to -3 ± 60 and -2 ± 80 mV, respectively. However, these values are still larger than the trimming range of the threshold, which is 5 mV per bit. In the present ASIC, the baselines can only be adjusted in a negative direction, and thus the distribution is asymmetric and broadens in the negative direction. The baseline distribution may be due to the dispersion in components caused by irregularities in the manufacturing process. Therefore, the adjustable ranges of the offset DACs and trim DACs must also be extended for practical use.

5. Measurements with a CdTe detector

To verify low-noise performance, the ASIC must be assembled together with a CdTe detector. The detector is based on the high-quality single CdTe crystal manufactured by ACRORAD of Japan. With the use of indium (In) and platinum (Pt) for the anode electrode and cathode electrode, respectively, this device works as a Schottky diode. This device has lower leakage current than ohmic detectors and allows higher bias voltages to be applied, leading to almost full charge collection [20]. Moreover, the cathode electrode is covered by a guard ring to reduce the leakage current of the detector [21]. The detector measures 2.4×2.4 mm in size and 0.5-mm thick, and is covered by a guard ring 1 mm in width.

Since the spectral performance depends on the leakage current and detector capacitance, the leakage current must be measured before connection with the ASIC. Positive voltages were applied to the indium electrode using a Keithley 237, and current on the cathode side was measured using a Keithley 6517A. As a result, the measured leakage current was 12 pA with a bias voltage of 600 V at 20 °C, and the detector capacitance was 1.2 pF.

Fig. 12 shows the setup for the spectral measurements. An electric wire of about 1 cm is used for connection

between the active area of the cathode electrode and the DIP socket mounted on the test board. The DIP socket is wired to the QFP-80 socket pins corresponding to the CSA input. We obtained the gamma-ray spectra of radioactive sources ^{241}Am (in Fig.13) and ^{57}Co (in Fig. 14) with C_f = 0.02 pF and self-trigger mode at an operating temperature of 20 °C and a bias voltage of 600 V. The channel peaking time was measured using the waveform before obtaining the spectra, and its value was 4.13 μs with the detector. The energy resolution is 2.51 keV (FWHM) for a gamma ray of 59.5 and 2.35 keV (FWHM) for a gamma ray of 122 keV. The test pulse spectra were obtained with an injected charge of 2 fC (equivalent to about 55.4 keV in the CdTe detector) and shifted in right direction for comparison. As for the ^{57}Co spectrum, the gain was carefully calibrated with a quadratic function, because the peak energy of 122 keV is around the maximum output swing of 1 V. Note here that common mode noise correction was not performed for the output amplitude of the ASIC.

According to the width of pedestal distribution, the observed noise is 259e$^-$ (rms), while the noise level of this channel without the detector is 212e$^-$ (rms). Thus, the noise residual is given as 149e$^-$($= \sqrt{(259)^2 - (212)^2}$). The contribution of the equivalent noise charge (Q_n^2) from the leakage current (I_d) is calculated by the first term of Eq. (7) as follows:

$$Q_n^2 = 12 \cdot \left[\frac{e^2}{nA \cdot ns}\right] \cdot I_d \cdot T_M \tag{8}$$

where the equivalent noise charge is expressed in electrons. If we assume $T_M = 3.93\,\mu s$ and $I_d = 12\,pA$, the noise contribution from the detector leakage current is 24e$^-$. This value is too small to explain the noise residual. The origin of the excess noise is being investigated, although we speculated that the parasitic capacitance, which may be caused by an assembly issue, is added to the total input capacitance. To address this assembly issue, we are now designing a low-noise ceramic carrier for the bare chip.

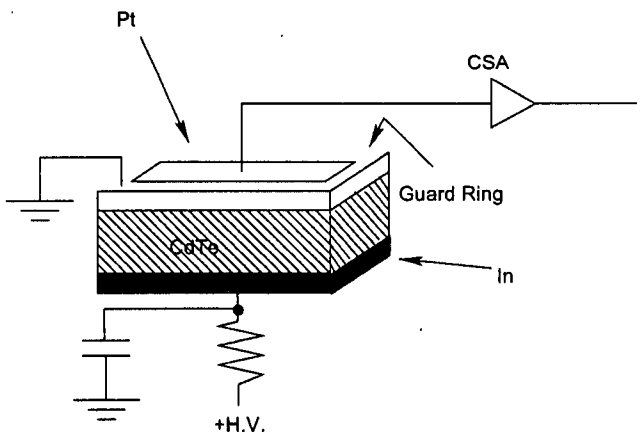

Fig. 12. Setup of the spectral measurements with a CdTe diode detector. The cathode face (Pt) is divided into the guard ring and the central plane (active area).

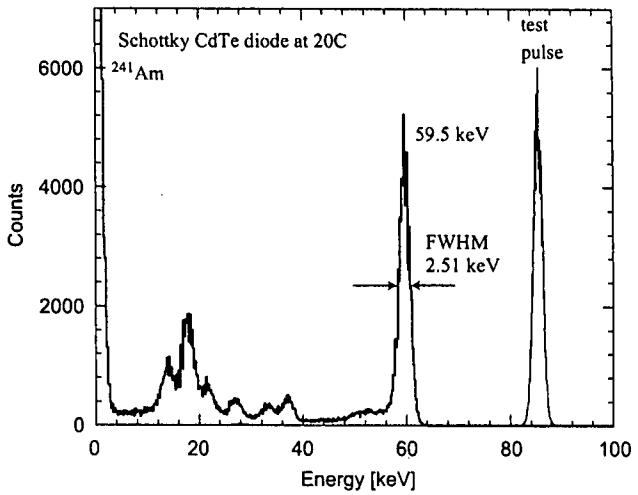

Fig. 13. Spectrum of ^{241}Am with the ASIC connected to a Shottky CdTe diode. The CdTe measures 2.4 × 2.4 × 0.5 mm in size and has a guard ring. The bias voltage is 600 V and operating temperature 20 °C.

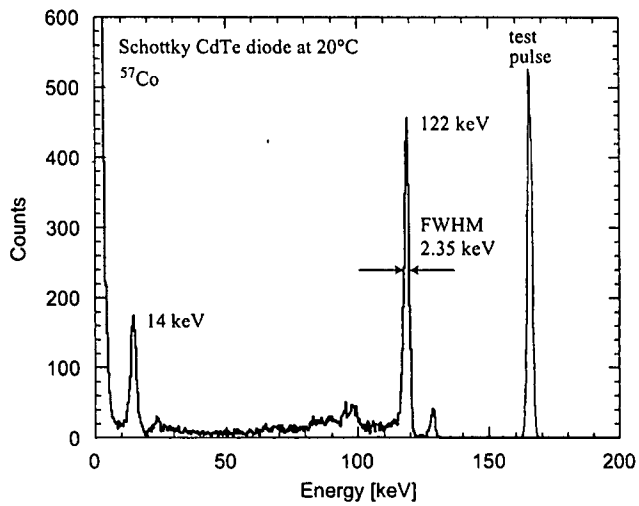

Fig. 14. Spectrum of ^{57}Co with the ASIC connected to a Shottky CdTe diode. This is obtained in the same condition as the spectrum of ^{241}Am.

6. Conclusion

We are developing low-noise front-end ASICs to read out CdTe detectors for future astrophysical applications. In order to establish low-noise circuit architectures, an eight-channel ASIC has been developed based on the Open-IP LSI project. By using the newly designed high-resistance circuit, the ASIC operates both for positive and negative signals with a wide dynamic range up to an input charge of 7 fC. The equivalent noise level of 188e$^-$ + 7.5e$^-$/pF (rms) has been reached for power consumption of 4 mW per channel. To verify the low-noise characteristics, we combined the ASIC with a CdTe diode detector